Fault Detection and Performance Analysis of Integrated Multi-Constellation GNSS/5G Positioning in Urban Environments

Yuan Zhang, *Graduate Student Member, IEEE,* Rui Wang, *Senior Member, IEEE,* and Erwu Liu, *Senior Member, IEEE*

Abstract—The integration of global navigation satellite systems (GNSS) and fifth generation (5G) for positioning integrity monitoring has recently become a significant research focus. However, as multi-constellation GNSS and ultra-dense 5G networks are deployed, the probabilities of fault is considerably high, requiring user receivers to safeguard against numerous fault modes resulting from various simultaneous independent faults. This study introduces a fast advanced receiver autonomous integrity monitoring (FARAIM) approach utilizing GNSS/5G integration, featuring a solution separation (SS) algorithm that avoids calculating fault-tolerant position solutions, thereby reducing the number of tests traditionally required. In the FARAIM framework, we discover that adding a single 5G measurement, along with the augmentation of cellular base station clock bias states into a multi-constellation GNSS, does not completely degrade the system's fault detection capabilities, as evidenced by the SS test's reduced performance and the consistency of the chi-square test. We derive a tighter *Gershgorin bound* for the FARAIM algorithm across the overall GNSS/5G measurements. Additionally, we analyze the protection level (PL) performance for adding a single 5G measurement. Finally, autonomous ground vehicle (AGV) experimental results validate the effectiveness of the proposed FARAIM algorithm in enhancing navigation performance and evalute theoretical findings regarding the influence of 5G measurements on integrity parameters.

Index Terms—Fifth-generation (5G), integrity monitoring, global navigation satellite systems (GNSS), protection level (PL), autonomous ground vehicle (AGV).

I. INTRODUCTION

IN critical safety applications such as aerospace, autonomous driving [1], [2], and unmanned aerial vehicles (UAVs) [3], [4], the accuracy and reliability of navigation systems are crucial. Multi-constellation global navigation satellite systems (GNSS) integrity monitoring [5] plays a crucial role in these domains to ensure the safety of both passengers and missions. This is especially relevant for autopiloted aircraft systems and UAVs, which are increasingly utilized in various civilian and military applications. For instance, procedures like localizer performance with vertical guidance (LPV-200) [6], which provides guidance down to 200 feet, require stringent standards for integrity, accuracy, and reliability to ensure robust navigation performance.

The presence of terrestrial-based cellular signals, including fifth generation (5G) [7]–[11] (known as new radio (NR)), offers a promising alternative or complement to traditional GNSS signals [12]. Integrating GNSS with 5G is necessary and advantageous [13], given GNSS's limitations in urban environments where signals are prone to interference, obstruction, and spoofing. Terrestrial-based signals can provide additional geometric diversity and enhance overall navigation performance. The anticipated increase in 5G base station (also known as next generation NodeBs or gNBs) density, projected to reach 40-50 stations per square kilometer, further supports the viability of this integration. There have been some relevant studies on integrating GNSS/5G positioning [14]–[19]. In our previous studies [16], [17], we introduced a novel particle filter estimation method to address the GNSS/5G integration positioning problem, specifically targeting 5G multipath issues. This method has been validated to demonstrate exceptional robustness. The work [18] introduced a multiple-rate adaptive Kalman filter (MRAKF) tailored for GNSS-5G hybrid positioning. This filter employs a sequential fusion scheme that integrates GNSS and 5G measurements at different data rates, thereby enhancing the use of high-rate 5G data. The study [19] aimed to detect GNSS spoofing attacks and help the user equipment recover its authentic position when only one gNB was available. In GNSS-challenging environments, the approach presented in [20] leveraged signals of opportunity (SOPs) in conjunction with a closed-loop map-matching strategy. Another method, highlighted in [1], involved an optimal path planning algorithm based on Dijkstra for autonomous ground vehicles (AGVs). This method optimizes the AGV path to minimize path length and position mean square error (MSE), while ensuring the position uncertainty and biases due to multipath effects remain within acceptable limits.

Emerging radio navigation applications, such as those for autonomous vehicles, increasingly depend on reliable positioning solutions. A reliable positioning solution ensures that position errors remain within a known protection level (PL) with a high degree of certainty. The computation of the PL must satisfy the performance requirement on the probability of hazardous misleading information (PHMI), which defines the probability that the positioning error exceeds the PL without the system issuing a timely alert. In radio navigation, calculating these error bounds is straightforward when the distribution of pseudorange errors is well-understood. When dealing with up to one measurement fault, receiver autonomous integrity monitoring (RAIM) [21]–[23] can be used to determine error bounds when up to one

measurement fault occurs. However, RAIM, originally designed for navigation, assumes that multiple measurement faults are unlikely, an assumption that does not hold in advanced RAIM (ARAIM) or navigation scenarios in complex environments. Factors such as multipath effects, clock errors (especially with terrestrial-based opportunistic signals), and spoofing can result in significant delays and increased probabilities of fault occurrences. For addressing GNSS satellite signal obstruction and multipath issues, the authors in [24] proposed leveraging 5G signals to assist in signal source integrity monitoring, thereby enhancing navigation performance. The opportunistic ARAIM (OARAIM) framework presented in [25] enhances fault detection and PL calculations by examining the effect of SOP integration on integrity performance. While previous research has extensively explored RAIM and ARAIM for GNSS/5G integrity monitoring, providing theoretical analysis and experimental validation for integrating wireless cellular measurements, the increased probabilities of faults due to the expanded data sources from multi-constellation GNSS and ultra-dense 5G networks significantly raise the computational burden of integrity monitoring. In such scenarios, traditional integrity monitoring algorithms are no longer practical [21].

ARAIM algorithms [26]–[28], developed for navigation, are designed to handle high fault probabilities. These algorithms typically generate a list of subsets corresponding to various fault modes (a fault mode being a combination of p simultaneous measurement faults), with associated probabilities. As the fault probability of each measurement increases, a greater number of subsets must be characterized. To compute the PL, the receiver needs to determine the position error covariance for each subset. While this approach is manageable for up to two simultaneous faults, it becomes unfeasible when the receiver needs to evaluate all subsets with $m-p$ measurements, particularly when $p \geq 3$, and m represents the total number of measurements. For instance, with $m = 30$, a target integrity level of 10^{-7}, and a fault probability of 1%, the receiver would need to evaluate 2 million subsets [29].

To address this challenge, several techniques have been proposed to reduce the number of subsets [30], [31], utilizing an effective method known as fault integration or fault grouping. This approach consolidates the list of faults into multiple groups, each of which is monitored by a single fault-tolerance solution. For ARAIM, this method has proven effective in scenarios with independent satellite or gNB fault modes. While fault grouping remains beneficial when the rate of constellation faults is substantially lower compared to independent satellite fault modes, it necessitates meticulous classification of fault categories. The authors in [32] introduced and evaluated a fast PL technique that monitored and addressed various subset geometries without directly calculating the corresponding fault-tolerant solutions or their covariances.

In this paper, we propose a fast ARAIM (FARAIM) PL computation framework based on the fast PL theory [32] of ARAIM. This framework combines GNSS and 5G signals to enhance fault detection, performance analysis, and PL computation. By addressing the complexities associated with high fault probabilities and challenging navigation environments, we aim to reduce the computational burden of PL calculations while analytically assessing the impact of adding 5G measurements into the GNSS measurement system on integrity.

This paper presents the following contributions, summarized as follows:

- We present a practical FARAIM algorithm for fault detection based on the integration of GNSS and 5G signals. This method demonstrates the use of a solution separation (SS) algorithm without computing the fault-tolerant position solutions when the probabilities of faults are randomly high, especially in the multi-constellation GNSS and ultra-dense 5G networks.
- Within the FARAIM framework, we find that adding a single 5G measurement, along with the augmentation of cellular base station clock bias states into a multi-constellation GNSS, does not completely degrade the system's fault detection capabilities, as evidenced by the SS test's reduced performance and the consistency of the chi-square test. We derived a tighter *Gershgorin bound* for the FARAIM algorithm across the overall GNSS/5G measurements. Furthermore, we also analyse the PL performance when a single 5G measurement is added to the GNSS system.
- Experiments with AGVs validate the effectiveness of the proposed FARAIM algorithm, showcasing improved navigation performance. These results also evaulte theoretical findings regarding the influence of 5G measurements on integrity parameters.

The structure of this paper is structured as follows: In Section II, we provide a model description. Section III presents a sensitivity analysis of fault detection in the GNSS/5G FARAIM user algorithm. Section IV offers a PL analysis of fault detection. Experimental results of the GNSS/5G integration are detailed in Section V. Finally, Section VI summarizes the analytical, simulation, and experimental findings of this paper.

II. MODEL DESCRIPTION

This section describes the pseudorange measurement models for GNSS and terrestrial-based 5G signals, as well as the weighted non-linear least squares (WNLS) estimator used for position estimation. The scenario involves an AGV navigating an urban environment, equipped with a receiver capable of generating pseudorange measurements from both GNSS satellites and nearby gNBs. Using these pseudorange measurements, the AGV can estimate its three-dimensional (3D) position, the receiver clock bias on the AGV, and the clock bias of the gNBs.

The AGV receives signals from N spatially stationary cellular gNBs. The coordinates of the cellular gNBs are assumed to be known a *priori* (e.g., through surveying and mapping or satellite imagery) and are stored in a locally hosted or cloud-based database accessible to the AGV. The three-dimensional location of the nth gNB is denoted by $\boldsymbol{r}_n^{\mathrm{gNB}}$, and signals are also received from M GNSS satellites, whose known positions are represented by $\boldsymbol{r}_m^{\mathrm{GNSS}}$.

A. GNSS Pseudorange Measurement

The AGV's receiver measures pseudoranges from the M GNSS satellites. Let $i \in \{1, \ldots, M_{\mathrm{const}}\}$ be the index of the independent constellation to which the mth GNSS satellite belongs. Therefore, the pseudorange measurement for the mth GNSS satellite is modeled as:

$$\rho_m^{\mathrm{GNSS}} = \|\boldsymbol{r} - \boldsymbol{r}_m^{\mathrm{GNSS}}\|_2 + c\left[\delta t_{m,i}^r - \delta t_m^{\mathrm{GNSS}}\right] + c\delta t_m^{\mathrm{iono}} + c\delta t_m^{\mathrm{tropo}} + v_m^{\mathrm{GNSS}},$$

$$(1)$$

where $\boldsymbol{r}$ is the unknown receiver position, c denotes the speed of light, $c\delta t^r_{m,i}$ represents the receiver clock error relative to the mth GNSS satellite and the ith GNSS constellation reference time, $\delta t^{\mathrm{GNSS}}_m$ denotes the satellite clock bias relative to the mth GNSS satellite. Additionally, $\delta t^{\mathrm{iono}}_m$ and $\delta t^{\mathrm{tropo}}_m$ represent the ionospheric and tropospheric delays, respectively. The measurement noise, denoted as v^{GNSS}_m, is modeled as a zero-mean Gaussian white noise with variance $\sigma^{\mathrm{GNSS}2}_m$. It is assumed that the measurement noises for different satellites are independent.

B. 5G Pseudorange Measurement

The positioning signals used in this study are obtained from the downlink signals within the 5G network. The channel impulse response (CIR) is simulated using ray-tracing techniques [7]. An orthogonal frequency division multiplexing (OFDM) symbol is transmitted over a multipath fading channel, assumed to remain constant for the duration of the symbol. The CIR can be expressed as follows

$$h(\tau) = \sum_{l=0}^{L-1} \alpha_l \delta(\tau - \tau_l), \qquad (2)$$

where L is the number of multipath components, α_l represents the relative attenuation, $\delta(\cdot)$ is the Dirac delta function, and τ_l denotes delay components of the lth path relative to the first path.

The CIR is crucial for deriving pseudorange measurements in a 5G environment. Once the CIR is obtained, it enables the calculation of the time of arrival (TOA) of signals from different paths. The first peak in the TOA, corresponding to the line-of-sight path, is used to estimate the distance between the receiver and the gNB. The receiver mounted on the AGV also makes pseudorange measurements for N 5G gNBs. The pseudorange measurement for the nth 5G gNB is modeled as:

$$\rho^{\mathrm{gNB}}_n = \|\boldsymbol{r} - \boldsymbol{r}^{\mathrm{gNB}}_n\|_2 + c\delta t^r - c\delta t^{\mathrm{gNB}}_n + v^{\mathrm{gNB}}_n, \qquad (3)$$

where v^{gNB}_n is the measurement noise, modeled as a zero-mean Gaussian white noise with variance $\sigma^{\mathrm{gNB}2}_n$. It is assumed that the measurement noises for different cellular gNBs $\{v^{\mathrm{gNB}}_n\}^N_{n=1}$ are independent.

Recent empirical study [25] shows that neighboring gNBs (especially those within the cellular network synchronization) maintain nominal synchronization, meaning the clock biases of different neighboring gNBs are dominated by a single common term. Assuming that the cellular gNBs are fully synchronized, the clock error measured by the nth cell can be expressed as:

$$c\delta t^{\mathrm{gNB}}_n = c\delta t^{\mathrm{gNB}}_1 + \epsilon_n + v_{\epsilon,n}, n = 2, ..., N, \qquad (4)$$

where ϵ_n denotes a constant deterministic bias, and $v_{\epsilon,\mathrm{n}}$ is considered a zero-mean white noise sequence with variance $\sigma^2_{\epsilon,\mathrm{n}}$. Note that $\nu_{\epsilon,n}$ denotes the synchronization noise associated with gNB timing alignment, while ν^{gNB}_n denotes the TOA measurement noise. These two terms are modeled as independent zero-mean white noise sequences. By substituting (4) into (3), the pseudorange measurement for the nth cellular gNB can be reformulated as:

$$\rho^{\mathrm{gNB}}_n = \|\boldsymbol{r} - \boldsymbol{r}^{\mathrm{gNB}}_n\|_2 + c\delta t^r - c\delta t^{\mathrm{gNB}}_1 - \epsilon_n + \acute{v}^{\mathrm{gNB}}_n, \qquad (5)$$

where

$$\acute{v}^{\mathrm{gNB}}_n \triangleq v^{\mathrm{gNB}}_n - v_{\epsilon}, n, n = 2, ..., N, \qquad (6)$$

where $v_{\epsilon,n}$ is considered a zero-mean Gaussian white noise with variance $\acute{\sigma}^{\mathrm{gNB}2}_n = \sigma^{\mathrm{gNB}2}_n + \sigma^2_{\epsilon,n}$.

The estimation of disturbances in the clock bias of cellular gNBs, including ϵ_n and $\sigma^2_{\epsilon,n}$, are discussed below:

Remark 1. *The constant bias ϵ_n and variance $\sigma^2_{\epsilon,n}$ can be estimated either locally by the AGV receiver or obtained from a cloud database. The difference between measurements is*

$$\rho^{\mathrm{gNB}}_1 - \rho^{\mathrm{gNB}}_n = \|\boldsymbol{r} - \boldsymbol{r}^{\mathrm{gNB}}_1\|_2 - \|\boldsymbol{r} - \boldsymbol{r}^{\mathrm{gNB}}_n\|_2$$
$$+ \epsilon_n + v^{\mathrm{gNB}}_1 - \acute{v}^{\mathrm{gNB}}_n. \qquad (7)$$

In practice, Eq. (7) is applied only during an initialization phase when the AGV is stationary in an open area with clear line-of-sight to GNSS satellites. In this scenario, the receiver position $\boldsymbol{r}$ can be accurately estimated, allowing the clock-bias disturbances to be obtained reliably. Once this initial calibration is complete, subsequent fault detection and positioning rely on relative clock measurements and do not require re-estimation of $\boldsymbol{r}$ under unknown conditions. Thus, the procedure remains feasible in practical deployments. If we assume the measurement noise is ergodic, then the constant bias ϵ_n and variance $\sigma^2_{\epsilon,n}$ can be computed using sample means and variances over K measurements:

$$\hat{\epsilon}_n = \frac{1}{K} \sum_{k_0=1}^{K} D_n(k_0), \qquad (8)$$

$$\hat{\sigma}^2_{\epsilon,n} = \left[\frac{1}{K-1} \sum_{k_0=1}^{K} [D_n(k_0) - \hat{\epsilon}_n]^2 \right] - \sigma^{\mathrm{gNB}2}_1 - \sigma^{\mathrm{gNB}2}_n. \qquad (9)$$

where k_0 denotes the time instant, $\hat{\epsilon}_n$, and $\hat{\sigma}^2_{\epsilon,n}$ are the estimated value, and

$$D_n(k_0) \triangleq \rho^{\mathrm{gNB}}_1 - \rho^{\mathrm{gNB}}_n - \|\boldsymbol{r} - \boldsymbol{r}^{\mathrm{gNB}}_1\|_2 + \|\boldsymbol{r} - \boldsymbol{r}^{\mathrm{gNB}}_n\|_2$$
$$= \epsilon_n + v^{\mathrm{gNB}}_1 - v^{\mathrm{gNB}}_n + v_{\epsilon,n}. \qquad (10)$$

Remark 2. *Although round-trip time (RTT) techniques can inherently cancel out clock biases via two-way message exchange, their applicability is constrained by system architecture. The present work considers one-way TOA measurements derived from 3GPP-compliant broadcast signals, such as the positioning reference signal (PRS), which are passively received without uplink support. RTT requires bidirectional communication and timestamp exchanges, which are infeasible in SOP-based or broadcast-only deployments. Moreover, in GNSS-challenged environments such as urban canyons and indoor spaces, 5G SOPs may lack synchronization or active communication capabilities, further limiting the feasibility of RTT. In contrast, TOA-based methods enable passive, low-complexity receivers and are compatible with scalable, infrastructure-independent positioning architectures. For these reasons, TOA is adopted in this study. Extension to RTT-based configurations will be considered in future work where infrastructure constraints allow.*

C. All-in-View Position Solution

The unknown state of the AGV is represented as $\boldsymbol{x} = \left[\boldsymbol{r}^\top, c\boldsymbol{\delta t}^{r\top}, c\delta t^r - c\delta t^{\mathrm{gNB}}_1 \right]^\top$, where $\boldsymbol{r}$ denotes the AGV's position, $c\boldsymbol{\delta t}^r = \left[c\delta t^r_1, ..., c\delta t^r_{M_{\mathrm{const}}} \right]^\top$ represents the receiver clock

bias for the M_{const} GNSS constellations, $c\delta t^r$ is the receiver clock bias for gNB, and $c\delta t_1^{\text{gNB}}$ is the clock bias of the first gNB.

A satellite or gNB is included in the all-in-view solution only if it has not been flagged within the last T_{RECOV} period (minimum time that a previously excluded GNSS satellite has been out of the all-in-view position solution) and if it possesses valid integrity support message (ISM) parameters, such as position, clock bias, and signal quality. The receiver position is then estimated by fusing GNSS and 5G pseudoranges and their respective time biases using a WNLS method. The combined GNSS-5G measurement vector $\boldsymbol{y} \in \mathbb{R}^{(N+M)\times 1}$ includes:

$$\boldsymbol{y} = \left[\rho_1^{\text{gNB}}, ..., \rho_N^{\text{gNB}}, \rho_1^{\text{GNSS}}, ..., \rho_M^{\text{GNSS}}\right]^\top. \quad (11)$$

Let $\hat{\boldsymbol{x}}$ be the estimate of $\boldsymbol{x}$, and $\hat{\boldsymbol{y}}$ the measurement update. A weighted least-squares estimation is conducted iteratively. The update for $\triangle\hat{\boldsymbol{x}}$ is provided by the following equation:

$$\triangle\hat{\boldsymbol{x}} = \left(\mathbf{H}^\top\mathbf{R}^{-1}\mathbf{H}\right)^{-1}\mathbf{H}^\top\mathbf{R}^{-1}\left(\boldsymbol{y} - \hat{\boldsymbol{y}}\right), \quad (12)$$

where $\mathbf{R} \in \mathbb{R}^{N\times M}$ denotes the measurement noise covariance, $\mathbf{H} \in \mathbb{R}^{(N+M)\times(4+M_{\text{const}})}$ is the measurement Jacobian evaluated at $\hat{\boldsymbol{x}}$ given by

$$\mathbf{H} = \begin{bmatrix} \mathbf{G} & \mathbf{T}^{\text{GNSS}} & \mathbf{0}_{M\times 1} \\ \mathbf{B} & \mathbf{0}_{N\times M_{\text{const}}} & \mathbf{1}_{N\times 1} \end{bmatrix}, \quad (13)$$

where $\mathbf{G} \in \mathbb{R}^{M\times 1}$ and $\mathbf{B} \in \mathbb{R}^{N\times 1}$ are geometry matrixs given by

$$\mathbf{G} = \begin{bmatrix} \frac{\boldsymbol{r}-\boldsymbol{r}_{\text{GNSS},1}}{\|\boldsymbol{r}-\boldsymbol{r}_{\text{GNSS},1}\|_2} \\ \vdots \\ \frac{\boldsymbol{r}-\boldsymbol{r}_{\text{GNSS},M}}{\|\boldsymbol{r}-\boldsymbol{r}_{\text{GNSS},M}\|_2} \end{bmatrix}, \mathbf{B} = \begin{bmatrix} \frac{\boldsymbol{r}-\boldsymbol{r}_{\text{gNB},1}}{\|\boldsymbol{r}-\boldsymbol{r}_{\text{gNB},1}\|_2} \\ \vdots \\ \frac{\boldsymbol{r}-\boldsymbol{r}_{\text{gNB},N}}{\|\boldsymbol{r}-\boldsymbol{r}_{\text{gNB},N}\|_2} \end{bmatrix}.$$

The augmented Jacobian matrix reveals that the receiver clock bias and nominal inter-base-station synchronization error are jointly absorbed into the final "1" entry, rendering them indistinguishable in the single 5G measurement case. Thus, the nominal inter-base-station synchronization assumption does not influence the following theoretical results. However, when multiple 5G measurements are incorporated, unmodeled inter-gNB clock offsets may introduce bias and degrade positioning accuracy. The (m,i)th entry of GNSS time matrix $\mathbf{T}^{\text{GNSS}} \in \mathbb{R}^{M\times M_{\text{const}}}$ is defined as

$$T_{m,i}^{\text{GNSS}} = \begin{cases} 1 & \text{if the } m\text{th satellite belongs to the } i\text{th constellation}, \\ 0 & \text{otherwise}. \end{cases} \quad (14)$$

To facilitate subsequent derivation, we define the weighting matrix $\mathbf{W} \in \mathbb{R}^{N\times M}$ as follows:

$$\mathbf{W} = \mathbf{R}^{-1} = \mathbf{C}_{\text{acc}}^{-1}, \quad (15)$$

where diagonal covariance matrices $\mathbf{C}_{\text{acc}}$ (see (16)) represents the nominal error model for integrity, which is used to assess system accuracy and continuity. The diagonal elements $\left\{C_{\text{acc}}^{-1}(t,t)\right\}_t^{M+N}$ ensure that the position estimates are precise and the navigation solution remains available without significant interruptions. The parameter σ_{URE} is the standard deviation of the clock and ephemeris error of GNSS satellite used for accuracy and continuity. The standard deviations of ionospheric and tropospheric residual errors are denoted by σ_{iono} and σ_{tropo}, respectively. The user error σ_{user} is computed following the model provided in [22] for Airborne Accuracy Designator—Model A.

III. FAULT DETECTION SENSITIVITY IN GNSS/5G FARAIM USER ALGORITHM

This section examines the impact of integrating 5G pseudoranges with GNSS pseudoranges on SS threshold test and chi-square threshold test. In scenarios where the number of ranging sources and fault rates are very high, such as with ARAIM in megaconstellations and 5G ultra-dense networks, standard approaches can become impractical. Most of these subsets, particularly those resulting from independent faults, exhibit strong geometries and contribute minimally to the integrity risk. To address this challenge, detection metrics such as the sum of squared residuals and SS test statistics are often employed to minimize the number of fault subsets. According to [32], it is unnecessary to compute the subset position solutions for measurement consistency checks, as the sum of squared normalized residuals (SSNR) conforms to a chi-square distribution.

According to [25], adding a single 5G pseudorange measurement reduces the fault detection sensitivity for all fault subsets when using only SS test statistics in the baseline ARAIM. Consider a subset Ω of the fault modes list, which includes all the $m-p$ subsets for a fixed p, where the subset solutions have not been computed. However, when adding the sum of square residuals for the subsets affected by independent faults $k \in \Omega$, we find that the chi-square threshold tests remain unchanged. For faulty subsets where $k \notin \Omega$, the SS test statistics increase. This means that the system's performance in fault detection sensitivity is not entirely compromised by adding a single 5G pseudorange measurement, provided both the sum of square residuals and SS test statistics are used together.

A. Detection Statistics and PL Calculations

In safety-critical applications, fault detection and exclusion (FDE) are inherently linked to PL or the integrity risk within an alert threshold. Identifying when measurements deviate from expected (nominal) errors is generally straightforward. The primary difficulty is to establish a dependable error bound PL when measurements appear consistent. This framework represents pseudorange errors through a set of mutually exclusive and collectively exhaustive fault hypotheses H_k, with H_0 indicating the fault-free condition. Each fault hypothesis introduces an unknown bias state b_k in one or more measurements and is paired with a known prior probability $p_{\text{fault},k}$. Let the direction index $q \in \{1,2,3\}$ represent the east, north, and up components, respectively. For each fault mode k and a given coordinate q, the PL is a scalar value ensuring that the integrity risk remains within the allocated threshold PHMI_q [32]:

$$P\left(|\hat{x}_q^{(0)} - x_q| > \text{PL}_q, \tau \leq T \mid H_k\right) \leq F\left(\frac{\text{PL}_q}{\sigma_q^{(0)}}, \frac{\sigma_{\text{ss},q}^{(k)}}{\sigma_q^{(0)}}, K\right), \quad (17)$$

where $\hat{x}_q^{(0)}$ is the estimated state of coordinate q under the fault-free hypothesis; $\boldsymbol{x}$ is the receiver position and clock states; T is a scalar value set to achieve a pre-defined false alert rate under fault-free conditions; τ is the SS test coefficient; F is an function that increases with the second argument; $\sigma_{\text{ss},q}^{(k)}$ is the standard deviation of the SS statistic; $\sigma_q^{(0)}$ is the standard deviation of the all-in-view position solution error, determined by the false alert probability requirement; K is the degrees of freedom, typically related to the test statistic used.

$$C_{\text{acc}}(t) = \begin{cases} \sigma^2_{\text{URE},t} + \sigma^2_{\text{tropo},t} + \sigma^2_{\text{iono},t} + \sigma^2_{\text{user},t}, & \text{if measurement } t \in \text{GNSS constellation,} \\ \sigma^2_{\text{URE},t} + \sigma^2_{\text{user},t}, & \text{otherwise.} \end{cases} \quad (16)$$

B. Monitoring Fault Modes and PL

To mitigate the combinatorial explosion in fault subset enumeration, FARAIM utilizes a unified upper bound on SS statistics derived from residual-based geometry. Specifically, the normalized separation can be conservatively bounded using a chi-squared threshold, avoiding the need to compute each fault mode individually. Fault modes are grouped into subsets Ω_j, each represented by a maximal standard deviation $\bar{\sigma}_q^{\Omega_j}$. The corresponding integrity risk is then evaluated analytically for each group, significantly reducing the number of tests while ensuring conservative PL computation.

The ARAIM algorithm detailed in [33] uses SS to monitor fault modes. Specifically, it ensures that for all

$$|\hat{x}_q^{(k)} - \hat{x}_q^{(0)}| \le T_{k,q} \text{ with } T_{k,q} = K_{\text{fa},q}^{(k)} \sigma_{\text{ss},q}^{(k)}, \quad (18)$$

where $\hat{x}_q^{(k)}$ is a fault-tolerant position solution for fault mode k, $K_{\text{fa},q}^{(k)}$ is false alarm allocation factor for fault mode k.

The PL_q can be provided by solving the equation:

$$2Q\left(\frac{\text{PL}_q}{\sigma_q^{(0)}}\right) + \sum_{k=1}^{N_{\text{fault}}} p_{\text{fault},k} Q\left(\frac{\text{PL}_q - T_{k,q}}{\sigma_q^{(k)}}\right) = \text{PHMI}_q, \quad (19)$$

where PHMI_q denotes the integrity budget to the qth coordinate; Q denotes the right-tail cumulative distribution function (CDF) of the normal distribution; $\sigma_q^{(k)}$ represents the standard deviation of the position solution error for the kth subset; N_{fault} is the total number of fault modes to monitor.

It has been proved in [22] that the square root of the sum of squared normalized residuals (SSNR) is a bound on the normalized solution separation. To efficiently reduce the number of tests, the relationship between normalized SS statistics and the SSNR is utilized. By utilizing this relationship, the computational burden can be significantly alleviated given by

$$\frac{|\hat{x}_q^{(k)} - \hat{x}_q^{(0)}|}{\sigma_{\text{ss},q}^{(k)}} \le$$
$$\sqrt{\boldsymbol{y}^\top \left(\mathbf{W} - \mathbf{W}\mathbf{H}\left(\mathbf{H}^\top \mathbf{W}\mathbf{H}\right)^{-1} \mathbf{G}^\top \mathbf{W}\right) \boldsymbol{y}}. \quad (20)$$

If a threshold $K_{fa}^{\chi^2}$ satisfies the following conditions:

$$\sqrt{\boldsymbol{y}^\top \left(\mathbf{W} - \mathbf{W}\mathbf{H}\left(\mathbf{H}^\top \mathbf{W}\mathbf{H}\right)^{-1} \mathbf{H}^\top \mathbf{W}\right) \boldsymbol{y}} \le K_{\text{fa},q}^{\chi^2}$$
$$= \sqrt{\left(\chi^2_{m-3-M_{\text{const}}}\right)^{-1} \left(1 - P_{\text{fa},\chi^2}\right)}, \quad (21)$$

where P_{fa,χ^2} is false alert allocation.

Then we are sure that we also have for any SS test

$$\frac{|\hat{x}_q^{(k)} - \hat{x}_q^{(0)}|}{\sigma_{\text{ss},q}^{(k)}} \le K_{\text{fa},q}^{\chi^2}. \quad (22)$$

Let N_Ω denote the the number of fault modes in Ω. If an upper bound $\bar{\sigma}_q^\Omega$ exists for all standard deviations $\sigma_q^{(k)}$ across all subsets

k in Ω, and for any value L, it is possible to compute a valid PL as described in [32]:

$$2Q\left(\frac{\text{PL}_q}{\sigma_q^{(0)}}\right) + \sum_{k \notin \Omega} p_{\text{fault},k} Q\left(\frac{\text{PL}_q - T_{k,q}}{\sigma_q^{(k)}}\right) +$$
$$\sum_{j=1}^{N_\Omega} \left(\sum_{k \in \Omega_j} p_{\text{fault},k}\right) Q\left(\frac{\text{PL}_q - K_{\text{fa},q}^{\chi^2} \sqrt{\bar{\sigma}_q^{\Omega_j 2} - \sigma_q^{(0)2}}}{\bar{\sigma}_q^{\Omega_j}}\right) = \text{PHMI}_q. \quad (23)$$

Fig. 1 shows the FARAIM algorithm flowchart, where the parameter user range accuracy σ_{URA} is a conservative representation of the unfaulted error distribution, $\boldsymbol{b}_{\text{nom}}$ denotes maximum nominal bias for satellite used for integrity and P_{const} is prior probability of a fault affecting more than one satellite in constellation. The algorithm first processes raw measurements and ISM data to generate navigation solutions. The core of the workflow is a sequence of statistical hypothesis tests (primarily the SS test and the chi-squared test) to detect and exclude potential faults. Based on the outcomes, PLs are calculated and compared against alert limits to either validate the final positioning results or trigger an integrity alarm.

C. Fault Detection Sensitivity Analysis of Integrated Multi-Constellation GNSS/5G Positioning

The system's fault detection sensitivity is not completely compromised by the addition of a single 5G pseudorange measurement, as long as both the sum of square residuals and SS test statistics are employed. This subsection builds on previous research by providing analytical insights into the performance degradation observed after the addition of a single gNB. The following two theorems assist in deriving and clarifying fault detection sensitivity in GNSS/5G positioning.

Although adding a single 5G pseudorange supplies one additional measurement, it also introduces a new unknown (the 5G clock bias), so the net degrees of freedom remain unchanged. Intuitively, one expects the position covariance to stay the same, as the extra equation is "paid for" by the extra state. However, because the new clock-bias state couples into the measurement Jacobian and information matrix, this intuition alone is not sufficient. The following **Theorem** III.1 provides a rigorous derivation, showing that marginalizing over the augmented state leaves the Fisher-information submatrix for position exactly the same as in the GNSS-only case. Hence, adding one 5G pseudorange measurement does not affect the position error or its uncertainty.

Theorem III.1. *Consider $M \ge 3 + M_{\text{const}}$ multi-constellation GNSS measurements for estimating the receiver's position $\boldsymbol{r}$ and clock bias $c\delta\boldsymbol{t}$. Adding an additional 5G measurement from an additional gNB and expanding the clock state vector $(c\delta t^r - c\delta t_1^{\text{gNB}})$ will not affect the position error or its uncertainty.*

Proof: See Appendix A. ∎

From **Theorem** III.1, it can be inferred that a minimum of $N \ge 2$ for multi-constellation GNSS/5G integration is necessary
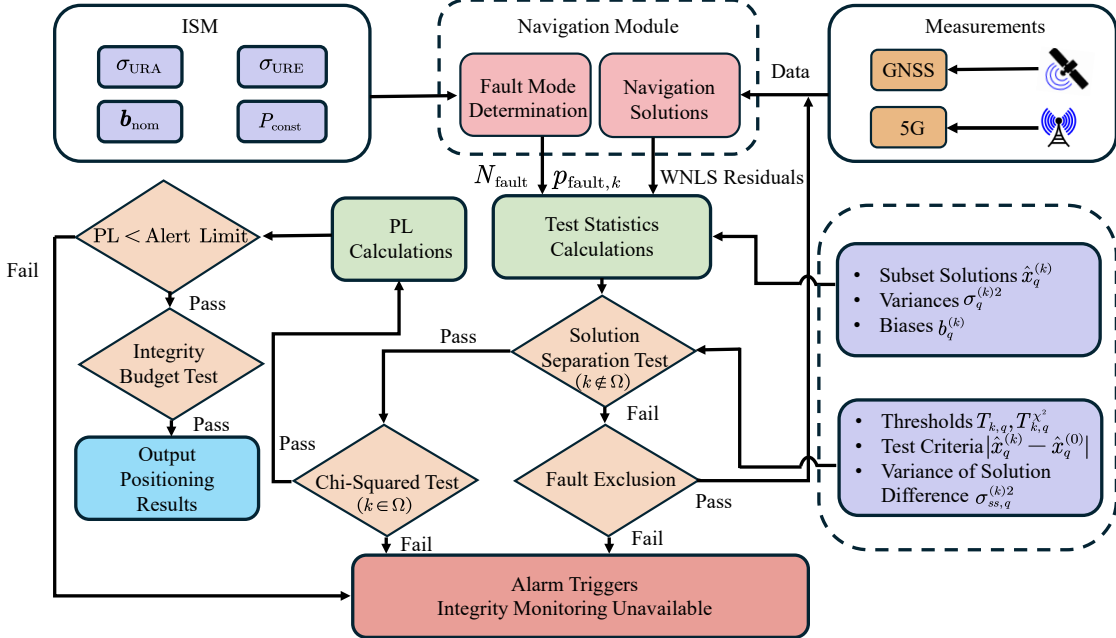
Fig. 1. Overview of FARAIM-based fault detection and exclusion for GNSS/5G integrated navigation systems.

to improve the position estimation. In practical scenarios (where only one 5G SOP is available or where that signal is not tightly synchronized with GNSS satellites) failing to model this 5G clock bias as a separate state renders the GNSS/5G observation model rank-deficient and unobservable. Explicitly augmenting the state vector with the 5G clock bias maintains a well-posed WNLS estimator and allows the combined system to distinguish GNSS clock errors from 5G clock errors. Although this additional measurement does not reduce position covariance, it increases redundancy by one, lowering the SS test threshold while leaving the chi-square threshold unchanged. This mismatch imposes an integrity-monitoring penalty when integrating a single asynchronous 5G measurement, which is not captured by analyses that assume fully synchronized measurements. A more detailed description is provided in **Theorem** III.2 below.

Remark 3. *As established in **Theorem** III.1, the inclusion of a single 5G pseudorange introduces an additional independent clock bias and does not contribute to position observability or reduce estimation uncertainty. Such a condition may arise when only one 5G SOP is present or when multiple SOPs lack inter-device clock synchronization. While this measurement appears geometrically redundant, it may have unintended consequences on integrity performance. Specifically, the added redundancy increases the system's degrees of freedom, thereby lowering the detection threshold in SS-based integrity monitoring. In contrast, the chi-squared detection threshold remains constant. This asymmetry can degrade fault detectability under multi-fault scenarios. To the best of our knowledge, this adverse effect has not been explicitly addressed in prior GNSS/5G integration studies and highlights a previously overlooked trade-off between redundancy and integrity reliability.*

A recent study [25] has demonstrated that including an additional pseudorange measurement from another gNB constellation can reduce the algorithm's sensitivity to faults in GNSS measurements. Nevertheless, adding a single 5G pseudorange measurement does not fully disable fault detection; it only reduces the SS test sensitivity, while the chi-square test remains unaffected. These theorems demonstrate the influence of a single 5G pseudorange measurement on integrity performance, particularly regarding fault detection sensitivity using both SSNR and SS test statistics.

Theorem III.2. *For GNSS/5G integration in fast PLs algorithms, a minimum of $M \geq 4 + M_{\text{const}}$ visible satellites and/or gNBs is generally required for integrity monitoring. Assume that the maximum number of faults is $p \geq 1$, representing the maximum simultaneous faults requiring monitoring, whether from satellites, gNBs, or constellations. Once p is set, all subsets with combinations of p or fewer events are generated. When adding a single 5G pseudorange measurement, the following effects are observed:*

1) *For a subset $k \notin \Omega$ of faulty configurations identified through SS threshold tests, increasing the scalar scale $T_{k,q}$ results in a decrease in the sensitivity of the GNSS/5G ARAIM system.*
2) *For subset $k \in \Omega$ within the list of fault modes detected by the chi-square test, chi-square threshold $T_{k,q}^{\chi^2} = \sigma_{\text{ss},q}^{(k)} K_{\text{fa},q}^{\chi^2}$ remains unaffected.*

Proof: See Appendix B. ∎

From **Theorem** III.2, it can be observed that the number of tests can be reduced by exploiting the relationship between the normalized SS statistics and the SSNR, thereby reducing the computational load. Furthermore, adding a single 5G pseudorange measurement does not fully compromise the system's fault detection capability, given that both the sum of squared residuals and SS test statistics are employed. **Theorem** III.2 extends the analysis to multiple simultaneous faults in GNSS/5G

measurements. Rather than addressing only the single-fault case, this result explicitly treats compound fault scenarios, which are critical for safety-critical applications. A closed-form relationship between solution-separation variance under fault and fault-free hypotheses significantly simplifies integrity analysis for multi-fault conditions. By jointly evaluating the sensitivity of both SS and chi-square detectors under various fault combinations, **Theorem III.2** offers a practical framework for ensuring robust integrity in hybrid GNSS/5G deployments, addressing requirements that single-fault treatments cannot satisfy.

IV. PLs ANALYSIS IN GNSS/5G FARAIM USER ALGORITHM

The first objective of this section is to establish an upper bound $\bar{\sigma}_q^{\Omega}$ for all σ_q^J, eliminating the need to enumerate all possible subsets in Ω, and further generalize this to a lower bound applicable in GNSS/5G scenarios. A shift in notation from index k to J has been made for more practical use in subsequent derivations. Note that $\nu_{\epsilon,n}$ denotes the synchronization noise associated with gNB timing alignment, while ν_n^{gNB} denotes the TOA measurement noise. These two terms are modeled as independent zero-mean white noise sequences. In the previous section, Ω represented an arbitrary subset of fault hypotheses. We now restrict Ω to include every fault hypothesis involving exactly p simultaneous faults. Under this specification, each fault hypothesis in Ω is identified by a set of p indices, denoted by J corresponding to the faulted measurements. The second objective of this section is to conduct a PL analysis following the inclusion of a single 5G pseudorange measurement.

A. Gershgorin bound

According to [32], for a subset position solution where indices j within set J have been removed, the standard deviation after applying the matrix inversion lemma $\bar{\mathbf{P}}$ is given by:

$$\sigma_q^{(J)2} = \sigma_q^{(0)2} + e^\top \mathbf{S}_J \left(\bar{\mathbf{P}}_{JJ} \right)^{-1} \mathbf{S}_J^\top e, \quad (24)$$

where $\bar{\mathbf{P}}_{JJ}$ is formed by selecting indices J from both the rows and columns of the matrix $\bar{\mathbf{P}} = \mathbf{W} - \mathbf{W}\mathbf{H} \left(\mathbf{H}^\top \mathbf{W}\mathbf{H} \right)^{-1} \mathbf{H}^\top \mathbf{W}$; $e^\top \mathbf{S}_J$ is derived by extracting the indices J of $e^\top \mathbf{S}_J$, where $\mathbf{S} = \left(\mathbf{H}^\top \mathbf{W}\mathbf{H} \right)^{-1} \mathbf{H}^\top \mathbf{W}$; The vector e projects the position onto the coordinate of interest. To normalize the matrix $\bar{\mathbf{P}}$ such that all diagonal terms are equal, we have

$$\sigma_q^{(J)2} = \sigma_q^{(0)2} + s_J \left(\bar{\mathbf{P}}_{JJ} \right)^{-1} s_J^\top, \quad (25)$$

where $s = \mathbf{D}^{-\frac{1}{2}} \mathbf{S}^\top e$ and s_J designates the vector obtained extracting the indices J in s, $\bar{\mathbf{P}} = \mathbf{D}^{-\frac{1}{2}} \bar{\mathbf{P}} \mathbf{D}^{-\frac{1}{2}}$, $\mathbf{D}$ is the matrix provided by the diagonal terms of $\bar{\mathbf{P}}$.

In [32], the authors provide an upper bound valid for any set J of a fixed size p given by

$$\max_{J \mathrm{s.t.}|J|=p} \sigma_q^{(J)2} \leq \sigma_q^{(0)2} + \frac{\max_{J \mathrm{s.t.}|J|=p} \|s_J\|^2}{\min_{J \mathrm{s.t.}|J|=p} \min \left(\lambda \left(\bar{\mathbf{P}}_{JJ} \right) \right)}, \quad (26)$$

where $|\cdot|$ denotes the number of elements in the set.

To achieve a tighter upper bound, it is necessary to generalize this upper bound to GNSS/5G scenarios. Consequently, a lower bound of $\min \left(\lambda \left(\bar{\mathbf{P}}_{JJ} \right) \right)$ must be provided.

Based on Gershgorin circle theorem [34], for any eigenvalue λ, we have

$$\min_i \left(a_{ii} - \sum_{j \neq i} |a_{ij}| \right) \leq \lambda. \quad (27)$$

Therefore, we obtain

$$\min_{i \in J} \left(\bar{P}_{ii} - \sum_{\substack{j \neq i \\ j \in J}} \left| \bar{P}_{ij} \right| \right) \leq \lambda \left(\bar{\mathbf{P}}_{JJ} \right). \quad (28)$$

We can now derive a lower bound that remains independent of the subset J while being dependent on its size p. For each row i of the normalized matrix $\bar{\mathbf{P}}$, the radius $Ra_i(p)$ is determined by subtracting the $p-1$ largest absolute off-diagonal coefficient from one. Formally, this can be expressed as

$$Ra_i(p) = |\bar{P}_{ii}| - \sum_{i \in J_{\max}(i)} \left| \bar{P}_{ij} \right|, \quad (29)$$

where $J_{\max}(i)$ denotes the set of indices in row i corresponding to the $p-1$ largest coefficients. Given that only these coefficients are included in the sum, we have:

$$Ra_i(p) \leq \bar{P}_{ii} - \sum_{\substack{j \neq i \\ j \in J}} \left| \bar{P}_{ij} \right|. \quad (30)$$

Therefore, we obtain

$$\min_{i \in [1,M]} \left(Ra_i(p) \right) \leq \min_{i \in J} \left(Ra_i(p) \right) \leq \lambda \left(\mathbf{P}_{JJ} \right). \quad (31)$$

When adding additional 5G measurements, we can get a lower bound compared to (31):

$$\min_{i \in [1,M+N]} \left(Ra_i(p) \right) \leq$$
$$\min_{i \in [1,M]} \left(Ra_i(p) \right) \leq \min_{i \in J} \left(Ra_i(p) \right) \leq \lambda \left(\mathbf{P}_{JJ} \right). \quad (32)$$

Using (26) and (32), we arrive at the following upper bound of $\sigma_q^{(J)2}$:

$$\max_{J \mathrm{s.t}|J|=p} \sigma_q^{(J)2} \leq \sigma_q^{(0)2} + \frac{\max_{J \mathrm{s.t}|J|=p} \|s_J\|^2}{\min_{i \in [1,M+N]} \left(Ra_i(p) \right)}. \quad (33)$$

Note that the left term in (33) is now independent of faulted subset J and is validated across the overall GNSS/5G measurements, which is precisely what we aimed to achieve. Additionally, it represents the smallest lower bound attainable using the *Gershgorin bound* method. This bound has been shown to be several orders of magnitude faster than computing the list of standard deviations, even when applying rank-one updates [32].

B. Protection Level Analysis with Additional 5G Measurement

It has been shown in [25] that adding a pseudorange measurement from an additional constellation in baseline ARAIM [22] leads to increased vertical and horizontal PLs. However, the impact of adding a gNB on integrity performance, specifically in terms of fast PLs for fault detection [32], a computationally efficient method, has not yet been explored. The following theorem elucidates the effect of adding a gNB on the computed PL.

TABLE I
SIMULATION SETTINGS

Parameters	Definition	Value
PHMI	Total integrity budget	10^{-7}
PHMI_v	Integrity budget for the vertical component	9×10^{-8}
PHMI_h	Integrity budget for the horizontal component	1×10^{-8}
$P_{\text{fa,v}}$	False alarm budget allocated to vertical direction	3.9×10^{-7}
$P_{\text{fa,h}}$	False alarm budget allocated to horizontal direction	9×10^{-8}
P_{THRES}	Threshold for the integrity risk coming from unmonitored faults	9×10^{-8}
P_{fa,χ^2}	Continuity budget allocated to the chi-square test	10^{-8}
α	Path loss exponent	3.48
$P_{\max}$	Maximum transmission power	$47\,\text{dBm}$
β	Path loss intercept	21.02
SF	Shadow fading	$2\sigma_{\text{SF}}$
γ	Path loss frequency dependence	2.34
N_0	Noise power spectral density	$-174\,\text{dBm/Hz}$
σ_{SF}	Shadow fading standard deviation	$6.5\,\text{dB}$
B	Bandwidth	$100\,\text{MHz}$
f	Carrier frequency	$30\,\text{GHz}$
N_{RB}	Number of resource blocks	66
G_{rx}	Receiver antenna gain	$0\,\text{dBi}$
F_{sc}	Subcarrier spacing	$120\,\text{kHz}$
MCL	Minimum coupling loss	70
N_{PRS}	Number of positioning reference signals	132
NF	Noise figure	$9\,\text{dB}$
N_a	Number of antennas	788

Theorem IV.1. *Assume that the maximum number of faults is $p \geq 1$, representing the maximum simultaneous faults requiring monitoring, whether from satellites, gNBs, or constellations. In a FARAIM framework, the total number of fault-detection tests can be reduced by leveraging the equivalence between normalized SS statistics and the SSNR. When a single 5G pseudorange measurement is included, the resulting PLs increase. Specifically, the analytically derived bound on $\bar{\sigma}_q^{\Omega_j}$ serves as a rigorous upper limit on the SS test variance. While this bound guarantees satisfaction of the PHMI requirement, the computed PL can be marginally greater than that of the baseline method.*

Proof: See in Appendix C. ∎

V. SIMULATION RESULTS

This section presents experimental results demonstrating the application of the proposed fast PL method within ARAIM for ground vehicle navigation, validating the sensitivity analysis of integrity performance using real GNSS signals in an urban environment. First, **Theorem** III.2 is confirmed by showcasing SS threshold tests and chi-square detection sensitivity both before and after the addition of a 5G pseudorange measurement along a given trajectory. Second, the PL analysis after adding gNBs as shown in **Theorem** IV.1 is demonstrated. Finally, a computational complexity analysis is provided. To illustrate the reduction in PLs

by adding 5G observations, we simulate ten additional 5G gNBs in the test environment and evaluate the resulting PL. Throughout the simulations presented in this section, the number of 5G gNBs was fixed at ten gNBs.

A. Experiment Setup

The raw GNSS measurements, after applying corrections for ionospheric and tropospheric errors, along with the 5G pseudorange measurements, are input into the WNLS estimator to compute the integrated GNSS/5G navigation solution. The integrity parameters and 5G configuration are consistent with those outlined in TABLE I. Fig. 2 illustrates the experimental setup, including the environment and hardware configuration. Detailed experimental parameter settings, including those for GNSS and 5G signals, are provided below.

1) GNSS Signal Setup: We used the ZED-F9P real-time kinematic (RTK) to generate a reference trajectory for validation purposes. It supports concurrent reception of GPS, GLONASS, Galileo, and BeiDou signals, ensuring robust and accurate positioning. The sampled dataset has a duration of about 10 min at a data rate of 1 Hz. Following standard practices for elevation angle masks, the number of visible satellites was determined with a maximum elevation mask of $15°$. The count of visible satellites is provided in Fig. 2, along with GNSS sky plots over
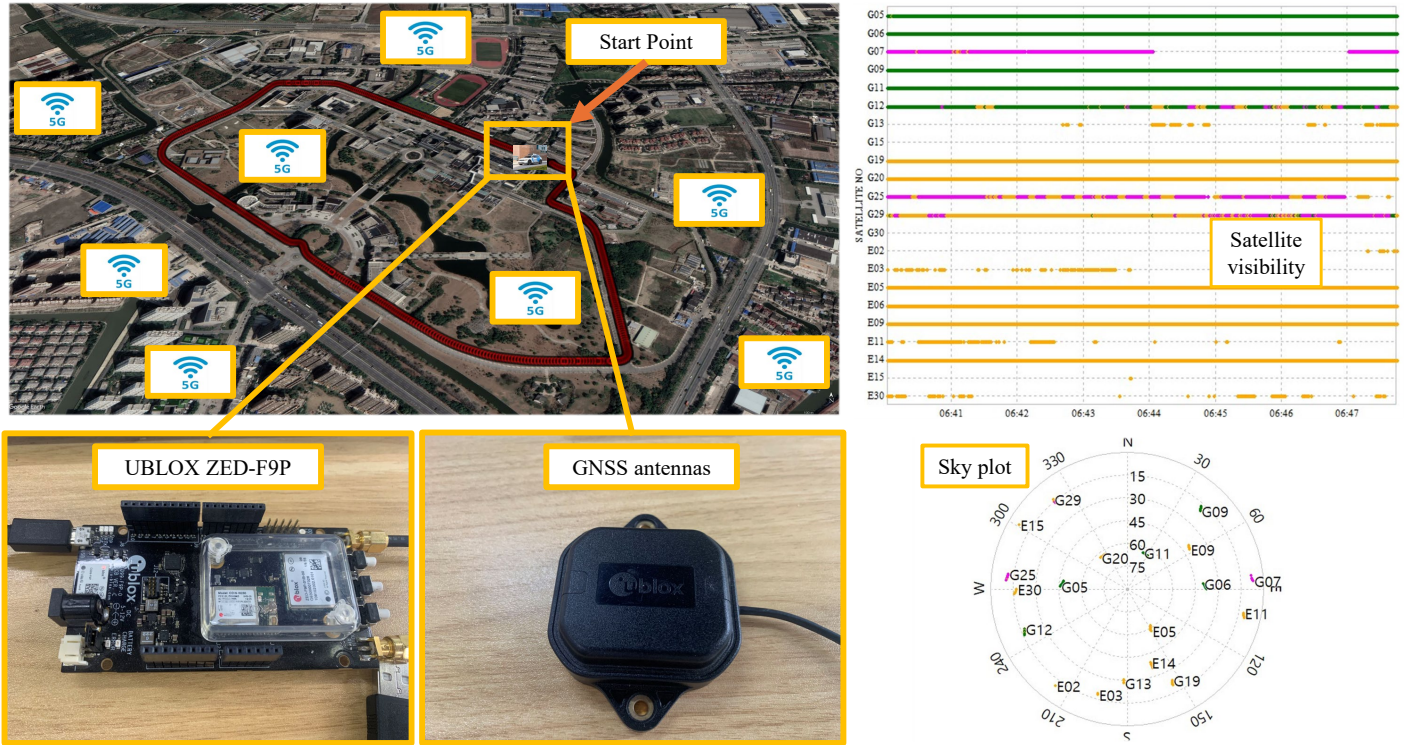
Fig. 2. Experimental setup, the AGV trajectory along with the position of 5G gNBs, satellite visibility, and the sky plot of GNSS satellite positions. Red lines indicate the AGV's trajectory, and white background rectangle frames indicate the 5G gNB layout.

the Tongji University Jiading Campus. The experiment utilizes observation and navigation RINEX files, version 3.00 or higher, and implements a single-point positioning technique with ARAIM, as detailed in earlier sections. The Saastamoinen and Klobuchar models [22] were used to mitigate tropospheric and ionospheric effects, respectively.

2) 5G Signal Setup: The 3rd generation partnership project (3GPP) technical report (TR) 38.855 specifies three deployment scenarios for gNBs: indoor office (IO), urban micro (UMi), and urban macro (UMa). This paper evaluates the performance of ARAIM technologies in 5G ultra-dense network environments, focusing on UMa gNBs. As outlined in [35], scenarios for 5G ultra-dense networks follow the simulation methodology established by the 3GPP working group, adding predefined environment parameters as shown in TABLE I. This simulation assesses the feasibility of 5G-based localization, generating numerical results under multipath channel conditions as defined in (2). In alignment with 3GPP Release 18 [35] positioning architecture, it is assumed that each gNB transmits PRS signals periodically, and the UE is capable of receiving downlink TOA measurements from multiple in-range gNBs. These measurements are acquired without requiring handovers or association with each gNB, as is typical in positioning-centric rather than communication-centric deployments.

For 5G systems, particularly with OFDM signals, the variance[1] of v_n^{gNB} can be calculated by

---

[1]According to [36], (34) is obtained from the CRLB of the time delay estimation.

$$\sigma_n^{\mathrm{gNB}\,2} = \mathrm{var}(v_n^{\mathrm{gNB}}) = \frac{c^2 T_s^2}{8\pi^2 \mathrm{SNR}_i \sum\limits_{i \in \mathcal{N}_{\mathrm{PRS}}} p_i^2 i^2}, \qquad (34)$$

where T_s represents the OFDM symbol duration. The signal-to-noise ratio SNR_n at the nth gNB, the subset of subcarriers dedicated to the positioning reference signal $\mathcal{N}_{\mathrm{PRS}}$, and the relative power weights p_i^2 of each subcarrier are essential parameters. More detailed 5G environment settings can be found in our previous studies [11], [16], [17], [37]. The MATLAB® ray tracing (RT) tool is utilized to conduct 5G positioning simulations in realistic urban environments. This tool [38] accurately models PRS and sounding reference signal (SRS) transmissions according to 3GPP Release 16 specifications, and simulates their propagation in 3D environments that account for the presence of buildings and associated multipath effects. The propagation environment can be configured to support an arbitrary number of reflections, enabling flexible analysis depending on the scenario. The 3D environment is rendered using the *site viewer* feature, which, in conjunction with the RT engine, facilitates the construction of realistic and reproducible positioning scenarios for system-level evaluations. Fig. 3 depicts an example setup, where an AGV, marked in blue, navigates within an area covered by two gNBs represented by red markers. In our simulation framework, the gNB positions are intentionally randomized within a predefined 3D volume encompassing the test area. This approach is adopted to evaluate the robustness and performance of our proposed algorithm under a wide and diverse array of geometric conditions, rather than limiting the analysis to a single, potentially idealized, deployment scenario.

This article has been accepted for publication in IEEE Transactions on Wireless Communications. This is the author's version which has not been fully edited and content may change prior to final publication. Citation information: DOI 10.1109/TWC.2025.3625223

10
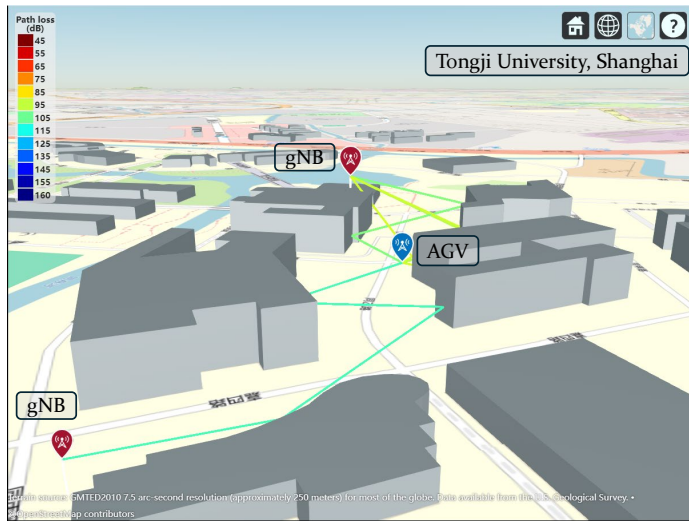
Fig. 3. Snapshot of the MATLAB® RT tool showing a simulated 5G positioning scenario at Tongji University, where an AGV (blue marker) navigates in an environment surrounded by two gNBs (red markers).

B. Detection Sensitivity Analysis

This subsection presents a comprehensive experimental validation of **Theorem** III.1 and **Theorem** III.2 through rigorous analysis of test statistics and thresholds in GNSS/5G hybrid positioning scenarios. To validate Theorem III.2, a comparative evaluation is conducted between GNSS-only pseudorange measurements and their augmented counterparts adding an additional 5G pseudorange observation.

To simplify the proof of **Theorem** III.2, we assume that the additional 5G measurement has a fault probability of zero. This assumption ensures that the classification of the original fault subsets remains unaffected. We then focus on a specific fault subset with the number 3, examining the changes in SS and chi-square detection thresholds, as well as the detection statistics, before and after the introduction of the 5G measurement.

TABLE II
EVALUATION OF **THEOREM** III.2: TEST STATISTICS, FALSE ALARM DISTRIBUTION COEFFICIENT, AND THRESHOLDS

Parameter	Direction	GNSS Only	GNSS + 5G
SS $K_{\mathrm{fa},q}^{(3)}$	$q = 1$	5.5293	5.5826
	$q = 2$	5.5293	5.5826
	$q = 3$	5.1374	5.1945
SS Test Thresholds	$q = 1$	0.5477	0.5529
	$q = 2$	0.2777	0.2803
	$q = 3$	2.4838	2.5114
$\sigma_{\mathrm{ss},q}^{(3)}$	$q = 1$	0.0991	0.0990
	$q = 2$	0.0502	0.0501
	$q = 3$	0.4835	0.4835
Chi-Square Test Statistics	$q = 1$	31.1721	31.1720
	$q = 2$	31.1721	31.1721
	$q = 3$	31.1721	31.1719
Chi-Square Test Thresholds	$q = 1$	0.5677	0.5675
	$q = 2$	0.3632	0.3633
	$q = 3$	3.4157	3.4157

TABLE II presents the test thresholds and statistics for the fault mode, showing that adding a single 5G measurement increases

the test threshold without altering the test statistics. Notably, the chi-square detection threshold remains almost unchanged, suggesting that the overall detection capability of the system is not completely compromised. This observation implies that the detection sensitivity for multiple-constellation GNSS fault modes is only partially reduced. These findings align precisely with the theoretical conclusions derived in **Theorem** III.1 and **Theorem** III.2, demonstrating their applicability in multi-source navigation systems.

C. Navigation Results and PL Analysis for Adding gNBs

This subsection presents navigation results and PL analysis for adding gNBs. The target operational level for ARAIM is LPV-200 [6], an emerging procedure not yet fully defined in the international civil aviation organization (ICAO) standards and recommended practices (SARPs). These standards provide comprehensive requirements and guidelines on positioning performance, continuity, and availability. Consequently, the related requirements and criteria must be met not only in a GNSS-only scenario but also in a GNSS/5G scenario. The SARPs describe four positioning performance criteria:

The SARPs outline four criteria for positioning performance [39]:

1) 4 meters vertical accuracy at 95%.
2) 10 meters vertical accuracy with 99.99999% fault-free assurance.
3) 15 meters vertical effective monitoring threshold (EMT) at 99.999% confidence.
4) Position error limits of 35 meters vertical and 40 meters horizontal, ensuring vertical PL (VPL) and horizontal PL (HPL) remain below 35 meters and 40 meters respectively, with 99.99999% confidence.

The time-varying estimation error curves for multi-constellation GNSS/5G navigation solutions are presented in Fig. 4. The horizontal error and vertical error is obtained by comparing the single-point positioning (SPP) solution with the ground truth obtained by RTK. The average horizontal error is approximately 2 meters, with a maximum error not exceeding 6 meters. Fig. 5 illustrates the position dilution of precision (PDOP) values in a multi-constellation GNSS/5G hybrid scenario over time. It can be observed that the implementation of ARAIM improves the PDOP values, particularly in situations with satellite blunders. Fig. 6 illustrates the HPL at the top and the VPL at the bottom for the GPS-only scenario. During certain intervals of the experimental sampling, the HPL reaches up to 700 meters, which clearly fails to meet the navigation requirements for LPV-200.

In contrast, Figs. 7 and 8 present the HPL and VPL for the GPS/5G and GNSS/5G scenarios, respectively. The introduction of additional 5G measurements in both the GPS/5G and multi-constellation GNSS/5G scenarios significantly reduces the HPL compared to the GPS-only scenario. Notably, the average HPL in the multi-constellation GNSS/5G scenario is approximately 4-5 meters, while the GPS/5G scenario averages around 7-8 meters. The former clearly satisfies the navigation performance requirements for LPV-200.

According to [25], adding a pseudorange measurement from another constellation to baseline ARAIM increases both vertical and horizontal PLs. Given that the fast PL for fault detection is a

This article has been accepted for publication in IEEE Transactions on Wireless Communications. This is the author's version which has not been fully edited and content may change prior to final publication. Citation information: DOI 10.1109/TWC.2025.3625223

11
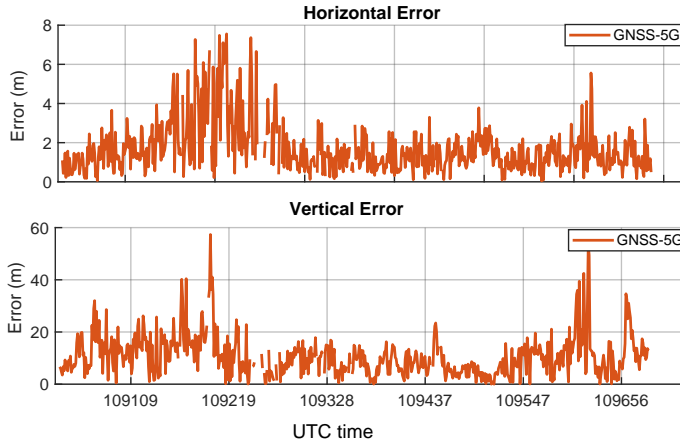
Fig. 4. Experimental comparisons of horizontal and vertical errors obtained from SPP with RTK ground truth.
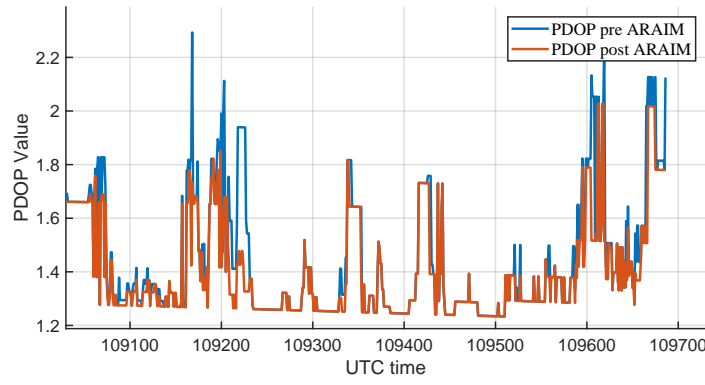
Fig. 5. Comparison of PDOP values for GNSS satellites and gNBs before and after the implementation of ARAIM.

Fig. 6. HPL (top) and VPL (bottom) for GPS scenario.
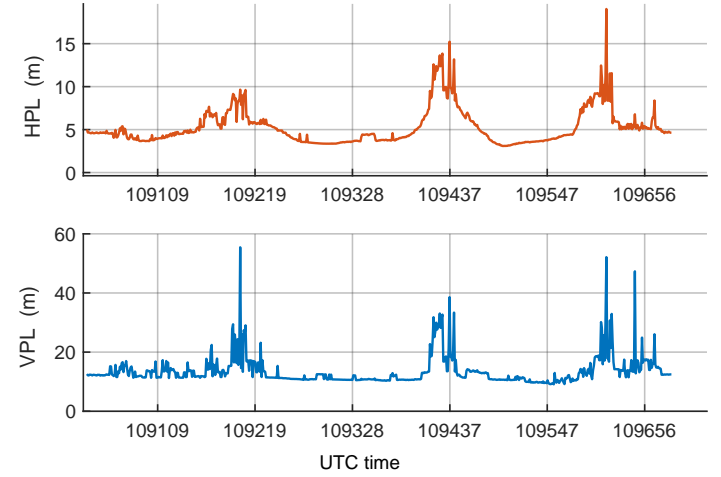
Fig. 7. HPL (top) and VPL (bottom) for GPS/5G hybrid scenario.

computationally efficient method, taking HPL as an example, Fig. 9 shows that the proposed method exhibits minimal performance loss on HPL compared to the baseline algorithm when a 5G measurement is added, which affirms **Theorem** IV.1. This highlights the advantages of the algorithm in multi-constellation GNSS/5G positioning. Not only does it theoretically reduce the ARAIM computation complexity, but it also has the potential to maintain performance comparable to the baseline method. The analysis here uses the HPL of GNSS only as a baseline to compare the impact of adding 5G measurements on HPL, as shown in Fig. 10. For scenarios involving two or more gNBs, the results indicate a reduction in HPL over the experiment trajectory. This indicates that as the number of measurements increases, the measurement redundancy also increases, which makes the HPL decrease. It is important to note that only up to four gNBs are plotted in Fig. 10 to maintain clarity in the visualization.

D. Complexity Analysis

In the exhaustive search algorithm, the number of matrix inversions required is given by $\binom{N+M}{p}$, where each matrix inversion entails approximately $\frac{2}{3}(4+M_{\text{const}})^3$ operations, with $4 + M_{\text{const}}$ representing the number of states. This results in a total computational load of $\frac{2}{3}m^3\binom{N+M}{p}$ operations [22]. For the *Gershgorin bound* approach, the matrix $\bar{\mathbf{P}}$, which emerges from the position solution, is not factored into the complexity estimate

due to its minimal contribution. Additionally, the proposed method necessitates various computational steps, including n square root operations, $2n^2$ divisions for normalization, n^2p operations to identify the $p-1$ largest coefficients per row, and another n^2p operations to calculate radii $Ra_i(p)$. Hence, the total computational effort amounts to approximately $2(p+1)n^2$ operations [32]. TABLE III provides numerical estimates of these operation counts, serving as a measure of computational complexity. It illustrates the anticipated efficiency gains relative to the number of satellites

TABLE III
COMPUTATIONAL COMPLEXITY COMPARISON OF THE BASELINE AND FARAIM APPROACHES FOR DIFFERENT SATELLITE + 5G MEASUREMENT CONFIGURATIONS

Subset depth/ Number of satellites + 5G		$p = 2$	$p = 3$	$p = 4$	$p = 5$
$N + M = 15$	Baseline	5,670	24,610	73,910	162,162
	FARAIM	1,350	1,800	2,250	2,700
$N + M = 25$	Baseline	16,200	124,200	683,100	2,869,020
	FARAIM	3,750	5,000	6,250	7,500
$N + M = 35$	Baseline	32,130	353,430	2,827,440	17,530,128
	FARAIM	7,350	9,800	12,250	14,700

This article has been accepted for publication in IEEE Transactions on Wireless Communications. This is the author's version which has not been fully edited and content may change prior to final publication. Citation information: DOI 10.1109/TWC.2025.3625223

12
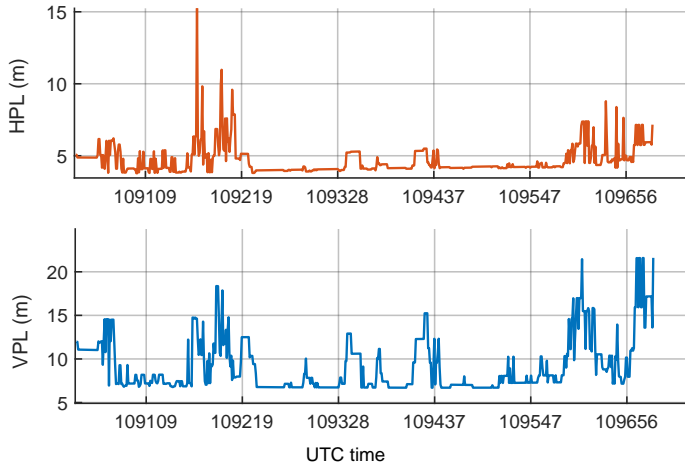
Fig. 8. HPL (top) and VPL (bottom) for multi-constellation GNSS/5G hybrid scenario.
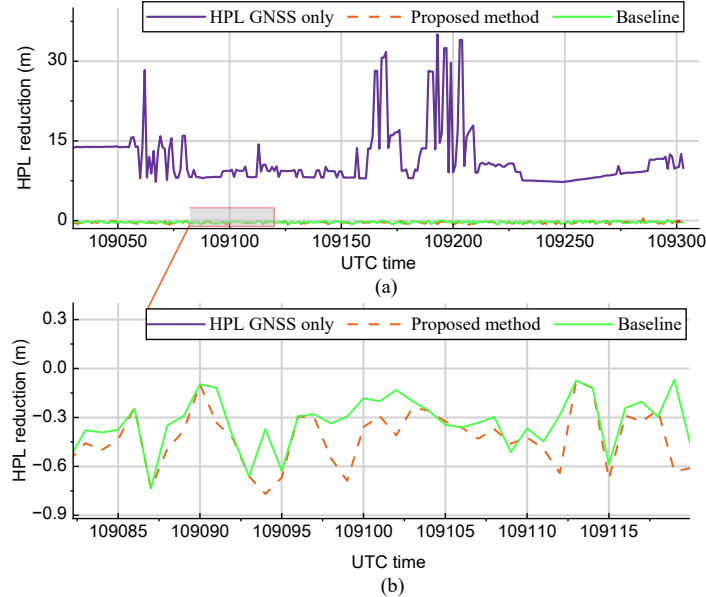
Fig. 9. (a) Time history of HPL reduction for adding one 5G measurement over the experimental trajectory. (b) A 50-second portion of HPL reduction for adding one 5G measurement over the experimental trajectory.

and gNBs (rows) and the maximum faulty subset size (columns).

VI. CONCLUSION

This paper proposed the FARAIM algorithm and analyzed the integrity performance of GNSS/5G integration. The increasing deployment of multi-constellation GNSS and ultra-dense 5G networks significantly raises the probability of fault occurrences, necessitating user receivers to protect against numerous fault modes from simultaneous independent faults. First, GNSS and 5G pseudorange measurement models were introduced, followed by the development of the FARAIM framework, which integrated gNBs with multi-constellation GNSS. The FARAIM approach employs a SS algorithm without calculating fault-tolerant position solutions, thus significantly reducing the number of required tests. We derived a tighter analytical *Gershgorin bound* for the FARAIM algorithm across the combined GNSS/5G measurements, achieving several orders of magnitude reduction in computational complexity
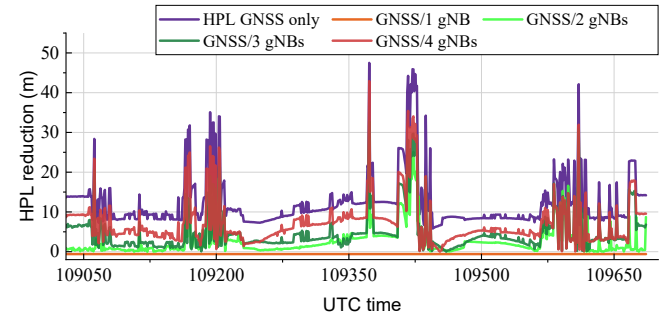

Fig. 10. HPL reduction for various gNB counts along the experimental trajectory.

compared to traditional enumeration-based standard deviation computations. Moreover, we demonstrated that the inclusion of a single 5G measurement and the augmentation of base station clock bias states do not necessarily degrade fault detection performance. This is evidenced by the preserved consistency of both the chi-square and SS tests. Additionally, we provided a detailed PL analysis under various GNSS/5G fusion scenarios, offering practical insights into how 5G measurements influence integrity-related thresholds. Finally, experimental validation using an autonomous ground vehicle confirmed the effectiveness and robustness of the proposed FARAIM algorithm in realistic environments, supporting the theoretical findings and demonstrating its potential for future safety-critical positioning applications.

Despite the promising results, a key limitation of the proposed approach lies in the conservative nature of the analytical *Gershgorin bound* under certain tightly coupled multi-fault conditions. While it enables fast evaluation, it may lead to loose thresholds that reduce detection sensitivity. Future work will focus on developing a branch-and-bound approach to better trade off between computational efficiency and tightness of integrity bounds.

APPENDIX A
PROOF OF THEOREM III.1

Proof: After the convergence of the WNLS iteration, the estimated state error $\boldsymbol{\varepsilon}$ is given by

$$
\begin{aligned}
\boldsymbol{\varepsilon} = \boldsymbol{x} - \boldsymbol{x}^{(\infty)} &= -\left(\mathbf{H}^\top \mathbf{R}^{-1} \mathbf{H}\right)^{-1} \mathbf{H}^\top \mathbf{R}^{-1}\left(\boldsymbol{y} - \hat{\boldsymbol{y}}^{(\infty)}\right) \\
&= -\left(\mathbf{H}^\top \mathbf{R}^{-1} \mathbf{H}\right)^{-1} \mathbf{H}^\top \mathbf{R}^{-1} \Delta \boldsymbol{y},
\end{aligned}
\tag{35}
$$

where $\Delta \boldsymbol{y}$ is the measurement residual vector, the state estimate after convergence is denoted by $\boldsymbol{x}^{(\infty)}$.

Therefore,

$$
\begin{aligned}
&\operatorname{Cov}\left(\boldsymbol{\varepsilon}, \boldsymbol{\varepsilon}\right) \\
&= \left(\mathbf{H}^\top \mathbf{R}^{-1} \mathbf{H}\right)^{-1} \mathbf{H}^\top \mathbf{R}^{-1} \operatorname{Cov}\left(\Delta \boldsymbol{y}, \Delta \boldsymbol{y}\right) \mathbf{R}^{-1} \mathbf{H}^\top \left(\mathbf{H}^\top \mathbf{R}^{-1} \mathbf{H}\right)^{-1} \\
&= \left(\mathbf{H}^\top \mathbf{R}^{-1} \mathbf{H}\right)^{-1} \mathbf{H}^\top \mathbf{R}^{-1} \mathbf{R} \mathbf{R}^{-1} \mathbf{H}^\top \left(\mathbf{H}^\top \mathbf{R}^{-1} \mathbf{H}\right)^{-1} \\
&= \left(\mathbf{H}^\top \mathbf{R}^{-1} \mathbf{H}\right)^{-1}.
\end{aligned}
\tag{36}
$$

This achieves the Cramér-Rao lower bound (CRLB) [40].

If range measurement errors are i.i.d., i.e., $\mathbf{R} = \sigma^2 \mathbf{I}$ with $\sigma = \sigma_1 = ... = \sigma_m$, we can separate the range errors from the geometric configuration. This decoupling is expressed by

$$
\operatorname{Cov}\left(\boldsymbol{\varepsilon}, \boldsymbol{\varepsilon}\right) = \left(\mathbf{H}^\top \mathbf{R}^{-1} \mathbf{H}\right)^{-1} = \sigma^2 \left(\mathbf{H}^\top \mathbf{H}\right)^{-1}.
\tag{37}
$$

This article has been accepted for publication in IEEE Transactions on Wireless Communications. This is the author's version which has not been fully edited and content may change prior to final publication. Citation information: DOI 10.1109/TWC.2025.3625223

13

Let's first consider a case involving only multi-constellation GNSS. The GNSS Jacobian matrix is given by

$$\mathbf{H}' = \begin{bmatrix} \mathbf{G} & \mathbf{T}^{\text{GNSS}} \end{bmatrix}. \tag{38}$$

The covariance matrix $\mathbf{P}'$ (also known as dilution of precision (DOP) inverse matrix [2]) is subsequently given by

$$\begin{aligned} \mathbf{P}' &= \left(\mathbf{H}'^{\top}\mathbf{H}'\right)^{-1} \\ &= \begin{bmatrix} \mathbf{G}^{\top}\mathbf{G} & \mathbf{G}^{\top}\mathbf{T}^{\text{GNSS}} \\ \mathbf{T}^{\text{GNSS}\top}\mathbf{G} & \mathbf{T}^{\text{GNSS}\top}\mathbf{T}^{\text{GNSS}} \end{bmatrix}^{-1} \triangleq \begin{bmatrix} \mathbf{A} & \mathbf{C} \\ \mathbf{C}^{\top} & \mathbf{D} \end{bmatrix}, \end{aligned} \tag{39}$$

where $\mathbf{A}$ is a 3×3 symmetric matrix, $\mathbf{C}$ is a $3 \times M_{\text{const}}$ matrix, and $\mathbf{D}$ is an $M_{\text{const}} \times M_{\text{const}}$ symmetric matrix.

In the least squares estimation, the state error vector $\boldsymbol{\varepsilon}$ is computed using the equation:

$$\boldsymbol{\varepsilon}' = -(\mathbf{H}'\mathbf{H}'^{\top})^{-1}\mathbf{H}'^{\top}\Delta\boldsymbol{y}, \tag{40}$$

where $\Delta\boldsymbol{y}' = \begin{bmatrix} \rho_1^{\text{GNSS}} - \hat{\rho}_1^{\text{GNSS}}, ..., \rho_M^{\text{GNSS}} - \hat{\rho}_M^{\text{GNSS}} \end{bmatrix}^{\top}$.

To proceed further, we obtain the estimated error given by

$$\boldsymbol{\varepsilon}' = \begin{bmatrix} \Delta\boldsymbol{r} \\ \Delta(c\delta\boldsymbol{t}) \end{bmatrix} = - \begin{bmatrix} \left(\mathbf{A}\mathbf{G}^{\top} + \mathbf{C}\mathbf{T}^{\text{GNSS}\top}\right)\Delta\boldsymbol{y}' \\ \left(\mathbf{C}^{\top}\mathbf{G}^{\top} + \mathbf{D}\mathbf{T}^{\text{GNSS}\top}\right)\Delta\boldsymbol{y}' \end{bmatrix}. \tag{41}$$

Using the matrix block inversion lemma, we have

$$\mathbf{A} = \left(\mathbf{G}^{\top}\boldsymbol{\Psi}\mathbf{G}\right)^{-1}$$
$$\mathbf{C} = -\left(\mathbf{G}^{\top}\boldsymbol{\Psi}\mathbf{G}\right)^{-1}\mathbf{G}^{\top}\mathbf{T}^{\text{GNSS}}\left(\mathbf{T}^{\text{GNSS}\top}\mathbf{T}^{\text{GNSS}}\right)^{-1}$$
$$\mathbf{D} = \left(\mathbf{T}^{\text{GNSS}\top}\mathbf{T}^{\text{GNSS}}\right)^{-1}$$
$$\left[\mathbf{I} + \mathbf{T}^{\text{GNSS}\top}\mathbf{G}\left(\mathbf{G}^{\top}\boldsymbol{\Psi}\mathbf{G}\right)^{-1}\mathbf{G}^{\top}\mathbf{T}^{\text{GNSS}}\left(\mathbf{T}^{\text{GNSS}\top}\mathbf{T}^{\text{GNSS}}\right)^{-1}\right]. \tag{42}$$

where $\boldsymbol{\Psi} \triangleq \mathbf{I} - \mathbf{T}^{\text{GNSS}}(\mathbf{T}^{\text{GNSS}\top}\mathbf{T}^{\text{GNSS}})^{-1}\mathbf{T}^{\text{GNSS}\top}$.

Therefore, the position error without 5G measurement is given by

$$\Delta\boldsymbol{r}' = -\left(\mathbf{G}^{\top}\boldsymbol{\Psi}\mathbf{G}\right)^{-1}\mathbf{G}^{\top}\boldsymbol{\Psi}\Delta\boldsymbol{y}'. \tag{43}$$

The augmented Jacobian matrix adding an additional 5G measurement is given by

$$\mathbf{H} = \begin{bmatrix} \mathbf{G} & \mathbf{T}^{\text{GNSS}} & \mathbf{0}_{M \times 1} \\ \boldsymbol{b}^{\top} & \mathbf{0}_{1 \times M_{\text{const}}} & 1 \end{bmatrix}, \tag{44}$$

where $\boldsymbol{b} \triangleq \frac{\boldsymbol{r} - \boldsymbol{r}_{\text{gNB},1}}{\|\boldsymbol{r} - \boldsymbol{r}_{\text{gNB},1}\|_2}$.

The augmented DOP matrix is given by

$$\mathbf{H}^{\top}\mathbf{H} = $$
$$\begin{bmatrix} \mathbf{G}^{\top}\mathbf{G} + \boldsymbol{b}\boldsymbol{b}^{\top} & \mathbf{G}^{\top}\mathbf{T}^{\text{GNSS}} & \boldsymbol{b} \\ \mathbf{T}^{\text{GNSS}\top}\mathbf{G} & \mathbf{T}^{\text{GNSS}\top}\mathbf{T}^{\text{GNSS}} & \mathbf{0}_{1 \times M_{\text{const}}} \\ \boldsymbol{b}^{\top} & \mathbf{0}_{1 \times M_{\text{const}}}^{\top} & 1 \end{bmatrix} = \begin{bmatrix} \mathbf{M} & \boldsymbol{m} \\ \boldsymbol{m}^{\top} & 1 \end{bmatrix}, \tag{45}$$

where

$$\mathbf{M} \triangleq \begin{bmatrix} \mathbf{G}^{\top}\mathbf{G} + \boldsymbol{b}\boldsymbol{b}^{\top} & \mathbf{G}^{\top}\mathbf{T}^{\text{GNSS}} \\ \mathbf{T}^{\text{GNSS}\top}\mathbf{G} & \mathbf{T}^{\text{GNSS}\top}\mathbf{T}^{\text{GNSS}} \end{bmatrix}, \boldsymbol{m} \triangleq \begin{bmatrix} \boldsymbol{b} \\ \mathbf{0}_{1 \times M_{\text{const}}} \end{bmatrix}.$$

[2]DOP is a term widely used in satellite navigation to represent the multiplicative effect of satellite geometry on positioning accuracy.

The augmented covariance is given by

$$\mathbf{P} = \left(\mathbf{H}^{\top}\mathbf{H}\right)^{-1} = \begin{bmatrix} \mathbf{E} & \boldsymbol{t} \\ \boldsymbol{t}^{\top} & a \end{bmatrix}, \tag{46}$$

where

$$\begin{aligned} \mathbf{E} &= \left(\mathbf{M} - \boldsymbol{m}\boldsymbol{m}^{\top}\right)^{-1} \\ \boldsymbol{t} &= -\left(\mathbf{M} - \boldsymbol{m}\boldsymbol{m}^{\top}\right)^{-1}\boldsymbol{m} \\ a &= 1 + \boldsymbol{m}^{\top}\left(\mathbf{M} - \boldsymbol{m}\boldsymbol{m}^{\top}\right)^{-1}\boldsymbol{m}. \end{aligned} \tag{47}$$

The matrix $\mathbf{E}$ may be written as

$$\begin{aligned} \mathbf{E} &= \left(\begin{bmatrix} \mathbf{G}^{\top}\mathbf{G} + \boldsymbol{b}\boldsymbol{b}^{\top} & \mathbf{G}^{\top}\mathbf{T}^{\text{GNSS}} \\ \mathbf{T}^{\text{GNSS}\top}\mathbf{G} & \mathbf{T}^{\text{GNSS}\top}\mathbf{T}^{\text{GNSS}} \end{bmatrix} - \begin{bmatrix} \boldsymbol{b}\boldsymbol{b}^{\top} & \mathbf{0} \\ \mathbf{0}^{\top} & \mathbf{0} \end{bmatrix}\right)^{-1} \\ &= \begin{bmatrix} \mathbf{G}^{\top}\mathbf{G} & \mathbf{G}^{\top}\mathbf{T}^{\text{GNSS}} \\ \mathbf{T}^{\text{GNSS}\top}\mathbf{G} & \mathbf{T}^{\text{GNSS}\top}\mathbf{T}^{\text{GNSS}} \end{bmatrix}^{-1} = \mathbf{P}', \end{aligned} \tag{48}$$

which implies that the uncertainty in position estimation remains unchanged with the addition of a 5G measurement. The corresponding error covariance can be written as

$$\mathbf{P} = \begin{bmatrix} \mathbf{P}' & -\mathbf{P}'\boldsymbol{m} \\ -\boldsymbol{m}^{\top}\mathbf{P}' & 1 + \boldsymbol{m}^{\top}\mathbf{P}'\boldsymbol{m} \end{bmatrix}. \tag{49}$$

We obtain the 5G integrated estimation error, which is given by

$$\Delta\boldsymbol{r} = -\mathbf{P}\mathbf{H}^{\top}\Delta\boldsymbol{y}, \tag{50}$$

where $\Delta\boldsymbol{y} = \begin{bmatrix} \Delta\boldsymbol{y}', \rho_1^{\text{gNB}} - \hat{\rho}_1^{\text{gNB}} \end{bmatrix}$.

By further organizing the matrices $\mathbf{P}$ and $\mathbf{H}$ and substituting them into equation (50), it can be verified that

$$\Delta\boldsymbol{r} = -\left(\mathbf{G}^{\top}\boldsymbol{\Psi}\mathbf{G}\right)^{-1}\mathbf{G}^{\top}\boldsymbol{\Psi}\Delta\boldsymbol{y} = \Delta\boldsymbol{r}'. \tag{51}$$

This implies that including an additional 5G measurement and expanding the gNB clock state vector $(c\delta t^r - c\delta t_1^{\text{gNB}})$ will not affect the position error or its uncertainty. ∎

APPENDIX B
PROOF OF THEOREM III.2

Proof: Let "new" represent the index after adding a single 5G pseudorange measurement and "old" represent the index within a multi-constellation GNSS system. Adding a single 5G pseudorange measurement increases the number of fault modes that require monitoring by a, i.e.,

$$N_{\text{fault,new}} = N_{\text{fault,old}} + a, \tag{52}$$

where $N_{\text{fault,new}}$ is the updated number of fault modes to be monitored, $N_{\text{fault,old}}$ is the old number of fault modes to be monitored in a multi-constellation GNSS. Here we assume that the maximum number of faults $p \geq 1$, the maximum number of simultaneous faults that require monitoring, including those from satellites, gNBs, or constellations. Once p is specified, all possible subsets involving combinations of p or fewer events are generated. If the receiver is required to enumerate all subsets containing $m - p$ measurements all subsets corresponding to the combination of p or fewer events are formed. When the receiver must list all subsets with $m - p$ measurements, then a should be calculated. If the original multi-constellation GNSS system has $N_{\text{fault,old}}$ fault modes, these modes include all possible single and combination faults.

This article has been accepted for publication in IEEE Transactions on Wireless Communications. This is the author's version which has not been fully edited and content may change prior to final publication. Citation information: DOI 10.1109/TWC.2025.3625223

14

After adding a new 5G pseudorange measurement, the new 5G measurement as a new fault source can appear as a single fault mode. Additionally, the new 5G measurement can combine with each existing fault mode to form new combination fault modes. The original system's fault modes total $N_{\text{fault,old}}$. A new 5G measurement adds 1 new single fault mode. The new 5G measurement can combine with each existing fault mode, adding $N_{\text{fault,old}}$ new combination fault modes. Thus, the total increase in fault modes a is

$$a = N_{\text{fault,old}} + 1. \tag{53}$$

According to **Theorem** III.1, adding an additional 5G measurement and expanding the clock state vector $(c\delta t^r - c\delta t_1^{\text{gNB}})$ will not affect the position error or its uncertainty, i.e.,

$$\hat{x}_{\text{new}}^{(k)} = \hat{x}_{\text{old}}^{(k)}, \sigma_{\text{new},q}^{(k)} = \sigma_{\text{old},q}^{(k)}, \sigma_{\text{new},q}^{(0)} = \sigma_{\text{old},q}^{(0)}. \tag{54}$$

As demonstrated in [32], when utilizing the all-in-view least squares position solution, the following identity holds:

$$\sigma_{\text{ss},q}^{(k)2} = \sigma_{q}^{(k)2} - \sigma_{q}^{(0)2}, \tag{55}$$

Therefore, we have

$$\sigma_{\text{new,ss},q}^{(k)2} = \sigma_{\text{new},q}^{(k)2} - \sigma_{\text{new},q}^{(0)2}. \tag{56}$$

Based on the above results (54), (55), (56) and [25], it can be readily shown that

$$\sigma_{\text{new,ss},q}^{(k)2} = \sigma_{\text{old,ss},q}^{(k)2}, \tag{57}$$

$$\hat{x}_{\text{new}}^{(k)} - \hat{x}_{\text{new}}^{(0)} = \hat{x}_{\text{old}}^{(k)} - \hat{x}_{\text{old}}^{(0)}. \tag{58}$$

For SS threshold coefficients for the new system, corresponding to a subset $k \notin \Omega$, they become

$$K_{\text{fa,new,1}} = K_{\text{fa,new,2}} = Q^{-1}\left[\frac{P_{\text{fa,h}}}{4(N_{\text{fault}} + a)}\right]$$
$$> K_{\text{fa,old,1}} = K_{\text{fa,old,2}}, \tag{59}$$
$$K_{\text{fa,new,3}} = Q^{-1}\left[\frac{P_{\text{fa,v}}}{2(N_{\text{fault}} + a)}\right] > K_{\text{fa,old,3}}.$$

where $P_{\text{fa,h}}$ and $P_{\text{fa,v}}$ are continuity budget allocated to the horizontal and vertical modes, respectively. Therefore, we have

$$T_{\text{new,k},q} > T_{\text{old,k},q}, k = 1, ..., N_{\text{fault}}. \tag{60}$$

For the chi-square test threshold, we have

$$\sqrt{\boldsymbol{y}^\top \left(\mathbf{W} - \mathbf{WH}\left(\mathbf{H}^\top \mathbf{WH}\right)^{-1}\mathbf{H}^\top \mathbf{W}\right)\boldsymbol{y}}$$
$$\leq K_{\text{old,fa},q}^{\chi^2} = \sqrt{\left(\chi_{m-3-M_{\text{const}}}^2\right)^{-1}(1 - P_{\text{fa}})}. \tag{61}$$

To proceed further, we obtain

$$K_{\text{new,fa},q}^{\chi^2} = \sqrt{\left(\chi_{m+1-3-M_{\text{const}}-1}^2\right)^{-1}(1 - P_{\text{fa}})} = K_{\text{old,fa},q}^{\chi^2}. \tag{62}$$

When the new system incorporates a 5G measurement and simultaneously augments the state vector $(c\delta t^r - c\delta t_1^{\text{gNB}})$, this does not change the degrees of freedom for the chi-squared distribution detection threshold. Thus, for $k = 1, ..., N_{\text{fault}}$, we can conclude that

$$T_{\text{new,k},q}^{\chi^2} = K_{\text{new,fa},q}^{\chi^2}\sigma_{\text{new,ss},q}^{(k)} = T_{\text{old,k},q}^{\chi^2}. \tag{63}$$

This means that the chi-squared distribution detection threshold of the new system has not changed. ∎

APPENDIX C
PROOF OF THEOREM IV.1

Proof: To simplify the analysis of the impact on PLs, we assume the probability of a fault in the newly added 5G gNB and the nominal biases are zero. Therefore, PHMI_q is constant. For the GNSS/5G integrity algorithm, the probability $P_{\text{fault,not monitored}}$ of fault modes not monitored remains unchanged:

$$P_{\text{new,fault,not monitored}} = P_{\text{old,fault,not monitored}}. \tag{64}$$

To show that the probability of unmonitored fault modes is invariant when a single 5G pseudorange is added, we explicitly note that each original fault mode retains its probability and that the new 5G-only fault mode has zero probability. The total probability of unmonitored faults therefore remains unchanged, and the corresponding term in the PL expression is identical before and after inclusion of the 5G measurement. Therefore, the PL with adding a 5G measurement can be computed using the following equation:

$$2Q\left(\frac{\text{PL}_{\text{new},q}}{\sigma_q^{(0)}}\right) + \sum_{k \notin \Omega} p_{\text{fault},k} Q\left(\frac{\text{PL}_{\text{new},q} - T_{k,q}}{\sigma_q^{(k)}}\right) +$$
$$\sum_{j=1}^{N_\Omega}\left(\sum_{k \in \Omega_j} p_{\text{fault},k}\right) Q\left(\frac{\text{PL}_{\text{new},q} - K_{\text{fa},q}^{\chi^2}\sqrt{\bar{\sigma}_q^{\Omega_j 2} - \sigma_q^{(0)2}}}{\bar{\sigma}_q^{\Omega_j}}\right)$$
$$= \text{PHMI}_q. \tag{65}$$

When a 5G measurement is added, $K_{\text{fa},q}^{\chi^2}$ in the third term on the left-hand side of the equal sign of (65) remains unchanged, and $\bar{\sigma}_q^{\Omega_j 2}$ increases. Considering inequality (60) and the monotonicity of the Q function yields the computed PL by adding one 5G measurement:

$$\text{PL}_{\text{new},q} > \text{PL}_{\text{old},q}, q = 1, 2, 3. \tag{66}$$

The key to the GNSS/5G ARAIM described in this section is the use of a computationally efficient method to compute the upper bound $\bar{\sigma}_q^{\Omega_j}$. For any value of PL and any k in Ω, we have

$$Q\left(\frac{\text{PL}_q - T_{k,q}}{\sigma_q^{(k)}}\right) \leq Q\left(\frac{\text{PL}_q - K_{\text{fa},q}^{\chi^2}\sqrt{\bar{\sigma}_q^{\Omega_j 2} - \sigma_q^{(0)2}}}{\bar{\sigma}_q^{\Omega_j}}\right). \tag{67}$$

Specifically, the analytically derived bound on $\bar{\sigma}_q^{\Omega_j}$ serves as a rigorous upper limit on the SS test variance. While this bound guarantees satisfaction of the PHMI requirement, the computed PL can be marginally greater than that of the baseline method. For a large number of satellites and/or gNBs, the bounds provided by the algorithm are often extremely tight [21]. In the following experiments, we show that the degradation in performance is very small. ∎

APPENDIX D
LIST OF ACRONYMS

5G	fifth generation
AGV	autonomous ground vehicle
ARAIM	advanced receiver autonomous integrity monitoring
FARAIM	fast ARAIM
GNSS	global navigation satellite system

LPV-200	localizer performance with vertical guidance 200
MRAKF	multiple-rate adaptive Kalman filter
MSE	mean square error
NR	new radio
OARAIM	opportunistic advanced receiver autonomous integrity monitoring
PHMI	probability of hazardous misleading information
PL	protection level
RAIM	receiver autonomous integrity monitoring
SOP	signal of opportunity
SS	solution separation
UAV	unmanned aerial vehicle
WNLS	weighted non-linear least squares
OFDM	orthogonal frequency division multiplexing
TOA	time of arrival
RTT	round-trip time
PRS	positioning reference signal
ISM	integrity support message
FDE	fault detection and exclusion
SSNR	sum of squared normalized residuals
CDF	cumulative distribution function
SSNR	sum of squared normalized residuals
RTK	real-time kinematic
3GPP	3rd generation partnership project
TR	technical report
IO	indoor office
UMi	urban micro
UMa	urban macro
ICAO	international civil aviation organization
SARPs	standards and recommended practices
EMT	effective monitoring threshold
VPL	vertical PL
HPL	horizontal PL
SPP	single-point positioning
PDOP	position dilution of precision
CRLB	Cramér-Rao lower bound
DOP	dilution of precision

REFERENCES

[1] S. Ragothaman, M. Maaref, and Z. M. Kassas, "Autonomous ground vehicle path planning in urban environments using GNSS and cellular signals reliability maps: Models and algorithms," *IEEE Trans. Aerosp. Electron. Syst.*, vol. 57, no. 3, pp. 1562–1580, 2021.

[2] G. Chen, B. Li, L. He, and T. Liu, "Enhanced land vehicular GNSS/INS combined system by using multiple-antenna with common clock," *IEEE Trans. Veh. Technol.*

[3] J. Khalife and Z. M. Kassas, "Precise UAV navigation with cellular carrier phase measurements," in *2018 IEEE/ION Position, Location and Navigation Symposium (PLANS)*, pp. 978–989. IEEE, 2018.

[4] K. Shamaei and Z. M. Kassas, "Sub-meter accurate UAV navigation and cycle slip detection with LTE carrier phase measurements," in *ION GNSS 2019*, pp. 2469–2479, 2019.

[5] A. Angrisano, S. Gaglione, N. Crocetto, and M. Vultaggio, "PANG-NAV: A tool for processing GNSS measurements in SPP, including RAIM functionality," *GPS Solut.*, vol. 24, no. 1, p. 19, 2020.

[6] B. DeCleene, "Performance requirements for LPV approaches to minima as low as 200 ft above runway threshold," in *International Civil Aviation Organization Navigation Systems Panel (NSP), Technical Working Group (WG1) Meeting*, 2006.

[7] K. Shamaei and Z. M. Kassas, "Receiver design and time of arrival estimation for opportunistic localization with 5G signals," *IEEE Trans. Wireless Commun.*, vol. 20, no. 7, pp. 4716–4731, 2021.

[8] A. A. Abdallah, K. Shamaei, and Z. M. Kassas, "Assessing real 5G signals for opportunistic navigation," in *ION GNSS+ 2020 Proceedings*, pp. 2548–2559, 2020.

[9] del Peral-Rosado *et al.*, "Achievable localization accuracy of the positioning reference signal of 3GPP LTE," in *2012 International Conference on Localization and GNSS*, pp. 1–6. IEEE, 2012.

[10] A. Abdallah, J. Khalife, and Z. M. Kassas, "Exploiting on-demand 5G downlink signals for opportunistic navigation," *IEEE Signal Process. Lett.*, vol. 30, pp. 389–393, 2023.

[11] Y. Zhang, R. Wang, and E. Liu, "Cooperative UAVs placement optimization for best multistatic time-of-arrival localization in 5G networks," *IEEE Trans. Wireless Commun.*, DOI 10.1109/TWC.2025.3532411, pp. 1–1, 2025.

[12] Z. Z. M. Kassas, J. Khalife, K. Shamaei, and J. Morales, "I hear, therefore i know where i am: Compensating for GNSS limitations with cellular signals," *IEEE Signal Process. Mag.*, vol. 34, no. 5, pp. 111–124, 2017.

[13] J. Gante, L. Sousa, and G. Falcao, "Dethroning GPS: Low-power accurate 5G positioning systems using machine learning," *IEEE J. Emerg. Sel. Topics Circuits Syst.*, vol. 10, no. 2, pp. 240–252, 2020.

[14] M. Brambilla, M. Alghisi, B. C. Tedeschini, A. Fumagalli, F. C. Grec, L. Italiano, C. Pileggi, L. Biagi, S. Bianchi, A. Gatti *et al.*, "Integration of 5G and GNSS technologies for enhanced positioning: an experimental study," *IEEE Open J. Commun. Soc.*, 2024.

[15] F. Campolo, A. Blaga, M. Rea, A. Lozano, and X. Costa-Pérez, "5GNSS: Fusion of 5G-NR and GNSS localization for enhanced positioning accuracy and reliability," *IEEE Trans. Veh. Technol.*, 2024.

[16] Y. Zhang, R. Wang, and Z. Xing, "A robust evolutionary particle filter technique for integrated navigation in urban environments via GNSS and 5G signals," *IEEE Trans. Ind. Inform.*, vol. 20, DOI 10.1109/TII.2024.3353849, no. 4, pp. 6866–6878, 2024.

[17] Y. Zhang, R. Wang, and Z. Xing, "Collaborative Navigation in Urban Environments via GNSS and 5G Signals," in *ICC 2023-IEEE International Conference on Communications*, pp. 6275–6280. IEEE, 2023.

[18] L. Bai, C. Sun, A. G. Dempster, H. Zhao, J. W. Cheong, and W. Feng, "GNSS-5G hybrid positioning based on multi-rate measurements fusion and proactive measurement uncertainty prediction," *IEEE Trans. Instrum. Meas.*, vol. 71, pp. 1–15, 2022.

[19] L. Bai, C. Sun, A. G. Dempster, H. Zhao, and W. Feng, "GNSS spoofing detection and mitigation with a single 5G base station aiding," *IEEE Trans. Aerosp. Electron.*, vol. 60, DOI 10.1109/TAES.2024.3382074, no. 4, pp. 4601–4620, 2024.

[20] M. Maaref and Z. M. Kassas, "Ground vehicle navigation in GNSS-challenged environments using signals of opportunity and a closed-loop map-matching approach," *IEEE Trans. Intell. Transp. Syst.*, vol. 21, no. 7, pp. 2723–2738, 2019.

[21] J. Blanch, S. Oak, S. Pullen, S. Lo, and T. Walter, " Advanced RAIM for mega-constellations," in *Proceedings of the 2024 International Technical Meeting of The Institute of Navigation*, pp. 258–271, 2024.

[22] J. Blanch, T. Walker, P. Enge, Y. Lee, B. Pervan, M. Rippl, A. Spletter, and V. Kropp, "Baseline advanced RAIM user algorithm and possible improvements," *IEEE Trans. Aerosp. Electron. Syst.*, vol. 51, no. 1, pp. 713–732, 2015.

[23] N. Zhu, J. Marais, D. Betaille, and M. Berbineau, "GNSS position integrity in urban environments: A review of literature," *IEEE Trans. Intell. Transp. Syst.*, vol. 19, no. 9, pp. 2762–2778, 2018.

[24] Y. Sun, L. Cao, S. Li, and Z. Deng, "G5gim: Integrity monitoring for GNSS/5G integrated navigation of urban vehicles," *IEEE Trans. Instrum. Meas.*, vol. 72, DOI 10.1109/TIM.2023.3298418, pp. 1–13, 2023.

[25] M. Jia, J. Khalife, and Z. M. Kassas, "Performance analysis of opportunistic araim for navigation with GNSS signals fused with terrestrial signals of opportunity," *IEEE Trans. Intell. Transp. Syst.*, vol. 24, DOI 10.1109/TITS.2023.3277393, no. 10, pp. 10 587–10 602, 2023.

[26] S. Luo, L. Wang, R. Tu, W. Zhang, J. Wei, and C. Chen, "Satellite selection methods for multi-constellation advanced RAIM," *Adv. Space Res.*, vol. 65, no. 5, pp. 1503–1517, 2020.

This article has been accepted for publication in IEEE Transactions on Wireless Communications. This is the author's version which has not been fully edited and content may change prior to final publication. Citation information: DOI 10.1109/TWC.2025.3625223

16

[27] Y. Zhai, B. Pervan, and M. Joerger, "H-ARAIM exclusion: requirements and performance," in *Proceedings of the 29th International Technical Meeting of the Satellite Division of The Institute of Navigation (ION GNSS+ 2016)*, pp. 1713–1725, 2016.

[28] T. Walter, J. Blanch, K. Gunning, M. Joerger, and B. Pervan, "Determination of fault probabilities for ARAIM," *IEEE Trans. Aerosp. Electron. Syst.*, vol. 55, no. 6, pp. 3505–3516, 2019.

[29] M. Joerger, F.-C. Chan, and B. Pervan, "Solution separation versus residual-based RAIM," *NAVIGATION: Journal of the Institute of Navigation*, vol. 61, no. 4, pp. 273–291, 2014.

[30] M. Orejas and J. Skalicky, "Clustered ARAIM," in *Proceedings of the 2016 International Technical Meeting of The Institute of Navigation*, pp. 224–230, 2016.

[31] M. Orejas, J. Skalicky, and U. Ziegler, "Implementation and testing of clustered ARAIM in a GPS/Galileo receiver," in *Proceedings of the 29th International Technical Meeting of The Satellite Division of the Institute of Navigation (ION GNSS+ 2016)*, pp. 1360–1367, 2016.

[32] J. Blanch and T. Walter, "Fast protection levels for fault detection with an application to advanced RAIM," *IEEE Trans. Aerosp. Electron. Syst.*, vol. 57, no. 1, pp. 55–65, 2020.

[33] J. Blanch, T. Walter, C. Milner, M. Joerger, B. Pervan, and D. Bouvet, "Baseline advanced RAIM user algorithm: proposed updates," in *Proceedings of the 2022 International Technical Meeting of The Institute of Navigation*, pp. 229–251, 2022.

[34] D. G. Feingold and R. S. Varga, "Block diagonally dominant matrices and generalizations of the gerschgorin circle theorem," *Pacific Journal of Mathematics*, vol. 12, no. 4, 1962.

[35] 3GPP, "Expanded and Improved NR Positioning," 3rd Generation Partnership Project (3GPP), Technical report (TR), 03 2021.

[36] J. A. del Peral-Rosado, J. A. López-Salcedo, S. Kim, and G. Seco-Granados, "Feasibility study of 5G-based localization for assisted driving," in *2016 International conference on localization and GNSS (ICL-GNSS)*, pp. 1–6. IEEE, 2016.

[37] Y. Zhang, R. Wang, E. Liu, B. Li, and H. Ge, "Asynchronous time-of-arrival-based 5G localization: Methods and optimal geometry analysis," *IEEE Internet Things J.*, DOI 10.1109/JIOT.2024.3435958, pp. 1–1, 2024.

[38] L. Italiano, B. C. Tedeschini, M. Brambilla, H. Huang, M. Nicoli, and H. Wymeersch, "A tutorial on 5G positioning," *IEEE Commun. Surv. Tutor.*, pp. 1–1, 2024.

[39] A. T. S. (2016), "Milestone 3 report," Working Group C, Technical report (TR), 02 2006.

[40] L. Heng and G. X. Gao, "Accuracy of range-based cooperative positioning: A lower bound analysis," *IEEE Trans. Aerosp. Electron. Syst.*, vol. 53, no. 5, pp. 2304–2316, 2017.

Rui Wang (Senior Member, IEEE) received the Ph.D. degree from Shanghai Jiao Tong University, China, in 2013. From August 2012 to February 2013, he was a Visiting Ph.D. Student with the Department of Electrical Engineering, University of California at Riverside. From October 2013 to October of 2014, he was with the Institute of Network Coding, The Chinese University of Hong Kong, as a Post-Doctoral Research Associate. From October 2014 to December 2016, he was with the College of Electronics and Information Engineering, Tongji University, as an Assistant Professor, where he is currently a Full Professor.

Dr. Wang received the Shanghai Excellent Doctor Degree Dissertation Award in 2015 and received the ACM Shanghai Rising Star Nomination Award in 2016. He has published over 60 articles. His research interests include wireless communications, artificial intelligence and wireless positioning. He is currently an Associate Editor of IEEE ACCESS and an Editor of the IEEE WIRELESS COMMUNICATIONS LETTERS.

Erwu Liu (Senior Member, IEEE) received the Ph.D. degree from the Huazhong University of Science and Technology, China, in 2001. He has been a Professor with Tongji University since 2011. Previously he was with Alcatel-Lucent from 2001 to 2007 and Imperial College London from 2007 to 2011.

He studies localization, blockchain, AI, and Internet of Things, with 120+ papers published and 70+ patents granted/pending. He won the Microsoft Indoor Localization Competition (IPSN) in 2016 and 2018, and developed the well-known indoor navigation system for China International Import Expo. He is the Community Dev. Co-Chair of IEEE Blockchain Technical Community, and leads the local group development of the IEEE BCTC in Asia/China. He leads the Shanghai Engineering Research Center for Blockchain Applications and Services. He is an IET Fellow, the Founding Editor-in-Chief of IET Blockchain, and the Founding Chair of the IEEE Global Blockchain Conference

Yuan Zhang (Graduate Student Member, IEEE) received the B.S. degree in surveying and mapping engineering with Shandong University of science and technology, Qingdao, China, in 2017, the M.S. degree in geodesy and surveying engineering with Jiangsu Normal University, Xuzhou, China, in 2020, and the Ph.D. degree in information and communication engineering from the College of Electronics and Information Engineering, Tongji University, Shanghai, China, in 2024. He is currently a Lecturer the School of Mechanical and Automotive Engineering, Anhui University of Engineering, Wuhu, China.

His research interests include GNSS/5G and multisensor integration for future accurate positioning. Additionally, he focuses on optimal sensor placement, estimation and optimization algorithms. He serves as a reviewer of several IEEE journals, including the IEEE Transactions on Wireless Communications, the IEEE Transactions on Industrial Informatics, the IEEE Transactions on Industrial Electronics, the IEEE Internet of Things Journal, the IEEE Signal Processing Letters and the IEEE Sensors Journal.